International Journal of Solids and Structures 193–194 (2020) 172–191

Contents lists available at ScienceDirect

International Journal of Solids and Structures

journal homepage: www.elsevier.com/locate/ijsolstr

Multiscale analysis and experimental validation of crack initiation in quasi-isotropic laminates

Yuta Kumagai[a], Sota Onodera[a], Marco Salviato[b], Tomonaga Okabe[a,c,*]

[a] Department of Aerospace Engineering, Tohoku University, 6-6-01 Aramaki-Aza-Aoba, Aoba-ku, Sendai, Miyagi 980-8579, Japan
[b] William E. Boeing Department of Aeronautics & Astronautics, University of Washington, 311D Guggenheim Hall, Seattle, WA 98195-2400, USA
[c] Department of Materials Science and Engineering, University of Washington, 302 Roberts Hall, Seattle, WA 98195, USA

ARTICLE INFO

Article history:
Received 10 November 2019
Revised 22 January 2020
Accepted 5 February 2020
Available online 13 February 2020

Keywords:
Composite materials
Crack
Fiber reinforced
Free edge
Laminate
Numerical methods

ABSTRACT

A multiscale approach comprising laminate-scale finite-element (FE) analysis and fiber-diameter-scale periodic unit cell (PUC) analysis was developed to predict matrix microcracking in quasi-isotropic laminates; further, this method was validated through comparison of our predictions with experimental results. In the mesoscopic FE analysis, the nonlinear deformation in the unidirectional laminae was incorporated to reproduce the deformation behavior of the laminate and obtain deformation histories at the locations of expected crack initiation in the laminate. In the microscopic analysis, the nonlinear behavior and crack initiation in the matrix resin were simply modeled by an elasto-viscoplastic law and a stress-based failure criterion, respectively. To predict crack initiation considering both the macroscopic deformation fields and the microscopic heterogeneity of the material, the mesoscopic FE analysis was conducted first. Subsequently, the microscopic PUC analysis was undertaken based on the strain histories obtained from the mesoscopic analysis. Our multiscale approach was applied to quasi-isotropic laminates with several laminate configurations to predict the matrix cracks in the 90° ply of the laminates. In addition to referring to experimental data cited in literature, initial and transverse cracks were observed when conducting tensile tests of quasi-isotropic laminates using the in situ replication technique and ex situ X-ray computed tomography. Through comparison of the predicted values with experimental results quoted in literature and obtained in this work, we validated the prediction capability of our multiscale analysis and evaluated the process of crack formation from the mesoscopic and microscopic points of view. Moreover, we examined the sensitivity of the predicted results to fiber arrangement and the influence of constitutive and failure modeling of the two-scale analysis on the predicted cracking strains. The reported method can predict initial and transverse cracks on quasi-isotropic laminates; further, it depicts the damage progress wherein microcrack nucleation and coalescence occurring before the full-width transverse cracking in laminated composites are observed under tensile loading conditions.

1. Introduction

In recent years, fiber-reinforced plastics (FRPs) have been applied to a wide range of products, such as aircraft, automobiles, and wind turbines, to achieve superior performance compared to that offered by conventional metal-based materials (Lukaszewicz, 2013; Rana and Fangueiro, 2016; Song and Gupta, 2012; Stenzenberger, 1993). In the aerospace industry, carbon fiber reinforced plastics (CFRPs) have been mainly used to fabricate structural components to reduce the weight of aircraft, which contributes to enhanced environmental friendliness and payload (Daniel and Ishai, 1994; Rana and Fangueiro, 2016). In aerostructures, CFRPs are primarily employed as laminates, manufactured from prepreg sheets consisting of carbon fibers and matrix resin. These structures have a hierarchical nature that ranges from the fiber-diameter scale to the structural component scale. The several length scales represent some of the causes of complex failure mechanisms of composite structures (Christensen, 2013; Talreja and Singh, 2012). To improve the design quality, performance, and safety of structures fabricated from laminated composites, accurate methods for the prediction of failure events for composites are essential.

From the failure prediction point of view, seizing the influence of the micro- and meso-structures on the damage evolution is key to capturing the dominant failure mechanisms. On the microscopic

* Corresponding author at: Department of Aerospace Engineering, Tohoku University, 6-6-01 Aramaki-Aza-Aoba, Aoba-ku, Sendai, Miyagi 980-8579, Japan.
E-mail address: okabe@plum.mech.tohoku.ac.jp (T. Okabe).

https://doi.org/10.1016/j.ijsolstr.2020.02.010
0020-7683/

scale, the heterogeneous microstructure comprising carbon fibers and matrix resin affects the microscopic stress/strain fields significantly. In fact, due to large material property differences between fibers and polymer matrix, large stress concentrations occur in the matrix phase leading to microscopic damage initiation and subsequent propagation (Asp et al., 1996a; Hobbiebrunken et al., 2006; Okabe et al., 2011). Since the foregoing microscopic damage can grow to mesoscopic damage e.g., in the form of transverse cracks and delaminations, it is important to predict damage initiation starting from the microscopic scale while accounting for material heterogeneity. Another aspect of utmost importance is the material anisotropy induced by the complex heterogeneous micro- and meso-structures. Although, if properly exploited, material anisotropy offers a great performance advantage over the isotropic nature of metals, it also causes complex deformation fields around the free edges of laminates (Lecomte-Grosbras et al., 2009; 2013; Okabe et al., 2015). These singular deformation fields can induce transverse cracks and subsequent delaminations, which can eventually lead to complete failure.

Considering these phenomena, computational models for the accurate evaluation of structural integrity must explicitly account for the nonlinear effects of material heterogeneity at the microscale and the laminate configuration at the mesoscale.

In the quest for an accurate failure prediction method for composite structures, numerous experimental and numerical studies have been performed on the microscopic and mesoscopic scales. In situ observations of transversely loaded composites by scanning electron microscopy (SEM) were performed to evaluate the onset of transverse cracks and the influence of voids on crack initiation (Hobbiebrunken et al., 2006; Aratama et al., 2016). X-ray micro-computed tomography was also used for detailed experimental observation to gain a better understanding of microscopic kink band formation, which is a fiber-dominant compressive failure mode, (Wang et al., 2017), mesoscopic transverse crack accumulation during tensile loading (Wright et al., 2008; Scott et al., 2012; Yang et al., 2015), and mesoscopic damage accumulation under fatigue conditions (Qiao et al., 2019; Qiao and Salviato, 2019). The digital image correlation (DIC) technique (Bornert et al., 2009), which enables measurement of the displacement and strain fields of the specimen, was employed to characterize free-edge strain fields of cross-ply (Okabe et al., 2015) and angle-ply (Lecomte-Grosbras et al., 2009; 2013) laminates. To predict the experimentally observed failure behavior, numerical approaches involving the dominant mechanisms of damage evolution have been developed. On the microscopic scale, representative volume elements (RVEs) consisting of carbon fibers and matrix resin were developed to predict the onset of matrix cracks and fiber/matrix debonding (Asp et al., 1996b; Melro et al., 2013; Elnekhaily and Talreja, 2018; 2019; Sudhir and Talreja, 2019), and kink band formation (Bai et al., 2015; Naya et al., 2017). On the mesoscopic scale, intralaminar and interlaminar cracks were predicted for several laminate configurations, using laminae having homogenized orthotropic properties with cohesive zone and/or continuum damage mechanics models (Su et al., 2015; Yang et al., 2015; Higuchi et al., 2017; Lu et al., 2018). In addition to numerical approaches, theoretical modeling, which contributes to establishing laminate behavior description, was performed to predict intralaminar crack accumulation (Ogihara et al., 2000; Singh and Talreja, 2010), stiffness degradation caused by intralaminar cracks (Carraro and Quaresimin, 2015; Onodera and Okabe, 2019), and delamination onset due to transverse cracks (Nairn and Hu, 1992; Carraro et al., 2017). These numerical and theoretical studies have contributed to establishing a better description of failure initiation and propagation and provided good predictions of failure strength and damage patterns in composite laminates. However, several limitations need to be overcome in order to improve the accuracy of the established models. In fact, microscopic analysis alone cannot reflect the complex deformation fields, due to the lack of upper scale data. On the other hand, due to homogenization of the fiber and matrix phases, mesoscopic analysis cannot address thermal-load-induced matrix deformation appropriately, which is known to affect the initial matrix-dominant failure significantly (Hart-Smith, 2014).

To address these challenges, multiscale formulations that account for both the microscopic and mesoscopic characteristics have been developed for problems related to damage prediction ranging from static to dynamic loadings (Souza et al., 2008; Sato et al., 2014; Okabe et al., 2015). These multiscale approaches employ two finite-element (FE) analyses on the different length scales: a microscopic analysis considering the heterogeneity of materials and a macroscopic analysis treating each lamina as homogeneous. By applying these methods to composite laminates, thickness-dependent cracking strains in cross-ply laminates (Okabe et al., 2015) and fiber-direction-dependent initial cracking strains in unidirectional laminates (Sato et al., 2014) have been successfully predicted. However, validation of a more practical configuration, such as quasi-isotropic laminates, has not been demonstrated in detail.

The transverse crack is one of the dominant damages in tensile-loaded composite laminates and was investigated in this study. According to extensive research undertaken on transverse cracking (Pagano et al., 1998; Okabe et al., 2015; Herráez et al., 2015; Yang et al., 2015; Zhuang et al., 2018; Kohler et al., 2019; Maragoni and Talreja, 2019), the process of a full-width transverse crack formation can be classified into three stages, as summarized in Fig. 1. At stage 1, nucleation of microcracks is induced near the free edge of the laminate by the free-edge stress concentration. At stage 2, coalescence of microcracks occurs owing to microcracks generated at stage 1 being connecting, which leads to free-edge crack formation. Finally, at stage 3, steady-state crack growth is initiated after energy criteria are satisfied, and then a full-width transverse crack is formed. The onset and propagation of such transverse cracks have been discussed for cross-ply laminates using a two-dimensional model (Okabe et al., 2008; Arteiro et al., 2014; Herráez et al., 2015). However, the prediction capability for the damage progress depending on laminate configurations has not been validated for quasi-isotropic laminates using a three-dimensional model.

In this study, a multiscale approach consisting of a laminate-scale FE analysis and a microscopic periodic unit cell (PUC) analysis was developed to predict the onset of matrix cracks in the 90° layer of quasi-isotropic laminates. A mesoscopic FE analysis that reproduced the nonlinear off-axis deformation of each ply was performed to obtain the deformation histories at the locations where matrix crack onset was most likely to occur. Then, a microscopic PUC analysis was conducted to predict matrix crack initiation based on the strain histories obtained from the mesoscopic analysis. In the microscopic analysis, material nonlinearity and crack initiation in the matrix phase were simply modeled by an elasto-viscoplastic law and a multiaxial stress-based failure criterion. Our multiscale analysis was applied to experiments on quasi-isotropic laminates reported in literature (Kobayashi et al., 2000; Ogihara et al., 2001) and those undertaken in this work to validate the prediction capability of the developed multiscale approach and discuss the cracking events in laminated composites with practical laminate configurations. For comparison with experimental data reported previously, nine laminate configurations including cross-ply and quasi-isotropic laminates were simulated to demonstrate the prediction capabilities for mesoscopic stress–strain behavior and laminate-configuration-dependent transverse cracking strains in the 90° layer of laminates. For further discussion of transverse crack prediction, detailed microscopic observation of initial and transverse cracking on three laminate configurations were conducted by the authors using the in situ replication

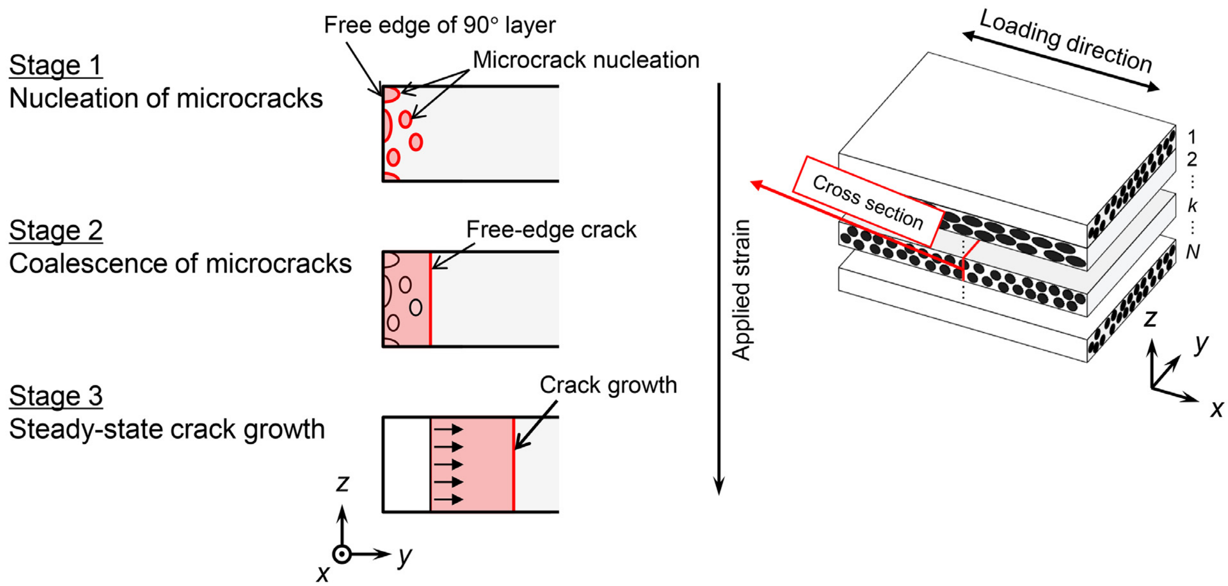

Fig. 1. Schematic illustration of transverse cracking process in 90° layer of composite laminate.

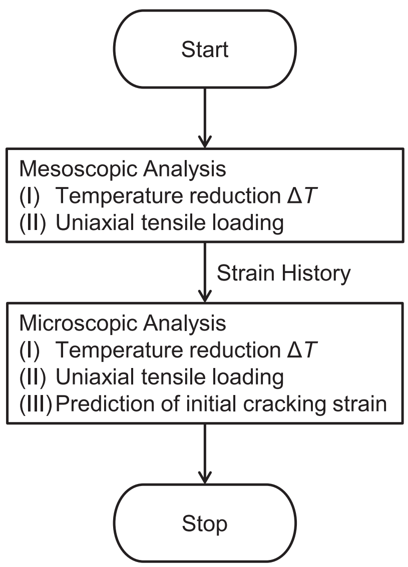

Fig. 2. Computational procedure for decoupled micro–macro multiscale analysis.

technique and ex situ X-ray computed tomography. The validity of our developed approach and cracking sequence in the 90° layer of quasi-isotropic laminates were discussed through the comparison of the predicted values with experimental observations.

2. Simulation methods

The strains at microcrack initiation in laminated composites were predicted by a multiscale approach that consists of laminate-scale finite-element (FE) analysis and fiber-diameter-scale periodic unit cell (PUC) analysis. Fig. 2 shows a flowchart summarizing the computational procedure of our multiscale analysis which features a micro–macro decoupling approach (Terada et al., 2014) to perform the two-scale analysis efficiently. The following subsections describe the mesoscopic and microscopic analyses and the simulation procedure.

2.1. Mesoscopic FE analysis of laminated composites

The laminae in a unidirectional CFRP composite under off-axis loading exhibit a nonlinear stress–strain behavior due to irreversible, nonlinear deformation in the matrix. The mesoscopic analysis was conducted leveraging an anisotropic elasto-plastic constitutive law proposed by Yokozeki et al. (Sun and Chen, 1989; Yokozeki et al., 2007) to capture the nonlinear behavior of the resin. In this constitutive law, the effective stress $\bar{\sigma}_{\mathrm{eff}}$ and yield function f are defined by the stress components associated with the principal material axes as follows:

$$\bar{\sigma}_{\mathrm{eff}} = \sqrt{\frac{3}{2}\left[(\sigma_{22}-\sigma_{33})^2 + 2a_{44}\sigma_{23}^2 + 2a_{66}\left(\sigma_{12}^2+\sigma_{13}^2\right)\right] + a_1^2\sigma_{11}^2} + a_1(\sigma_{11}+\sigma_{22}+\sigma_{33}), \quad (1)$$

$$\bar{\sigma}_{\mathrm{eff}} = \sqrt{3f}, \quad (2)$$

where the subscript 1 represents the fiber axis direction, the subscript 2 represents the in-plane transverse direction, and the subscript 3 represents the out-of-plane transverse direction. The yield function f given by Eq. (2) was used as the plastic potential for the flow rule (Sun and Chen, 1989) with the material parameters a_{44}, a_{66}, and a_1 governing the plastic behavior. Following Sato et al. (2014), the values $a_{44} = 2.0$, $a_{66} = 1.6$, and $a_1 = 0.01$ were adopted in this work.

The relationship between the effective stress $\bar{\sigma}_{\mathrm{eff}}$ and the effective plastic strain $\bar{\varepsilon}^{\mathrm{p}}_{\mathrm{eff}}$, which follows a Ramberg–Osgood model (Ramberg and Osgood, 1943), can be expressed as follows:

$$\begin{cases} \bar{\varepsilon}^{\mathrm{p}}_{\mathrm{eff}} = A_1(\bar{\sigma}_{\mathrm{eff}})^{n_1} & \text{for} \quad \bar{\sigma}_{\mathrm{eff}} < \bar{\sigma}^{\mathrm{threshold}}_{\mathrm{eff}} \\ \bar{\varepsilon}^{\mathrm{p}}_{\mathrm{eff}} = A_2(\bar{\sigma}_{\mathrm{eff}})^{n_2} & \text{for} \quad \bar{\sigma}_{\mathrm{eff}} \geq \bar{\sigma}^{\mathrm{threshold}}_{\mathrm{eff}} \end{cases} \quad (3)$$

where A_1, n_1, A_2, and n_2 are parameters to be fitted against the experimental uniaxial stress–strain curve. Two sets of parameters were used in the same way as reported in literature (Weeks and Sun, 1998) for accurate reproduction of nonlinear behavior. In this study, we assumed $A_1 = 3.2 \times 10^{-11}$, $n_1 = 3.8$, $A_2 = 4.5 \times 10^{-18}$, $n_2 = 7.0$, and $\bar{\sigma}^{\mathrm{threshold}}_{\mathrm{eff}} = 138$ MPa, as reported by Sato et al. (2014). A list of all the material properties used in the mesoscopic analysis is provided in Table 1.

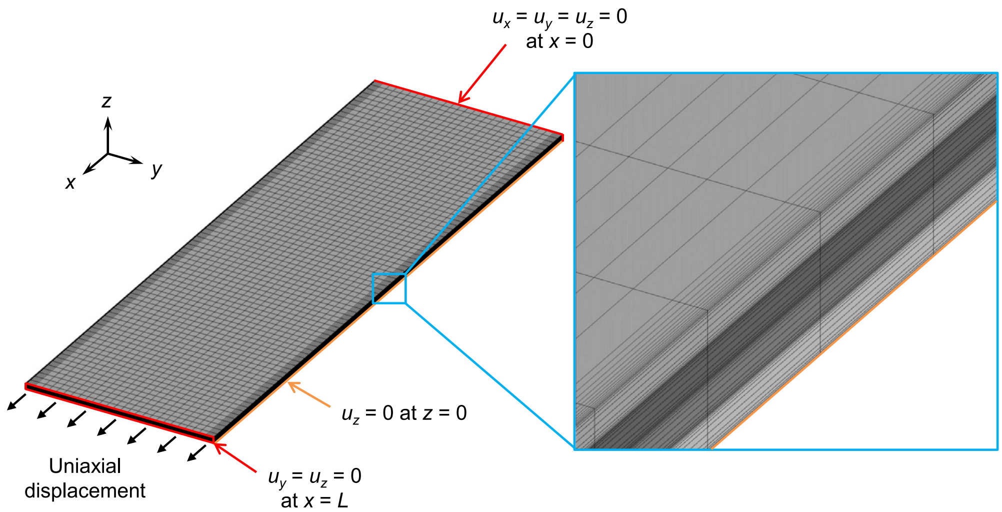

Fig. 3. Finite-element model used for macroscopic analysis showing the applied boundary conditions. The insert shows a detail of the three-dimensional mesh adopted in this model.

Table 1
Material properties used in mesoscopic FE analysis.

Material constant	a_{44}	2.0
	a_{66}	1.6
	a_1	0.01
	A_1	3.2×10^{-11}
	n_1	3.8
	A_2	4.5×10^{-18}
	n_2	7.0
	$\bar{\sigma}_{\mathrm{eff}}^{\mathrm{threshold}}$	138 MPa

A typical FE model used in the mesoscopic analysis is shown in Fig. 3, which shows that each lamina was modeled as a homogeneous anisotropic body with fiber angles assigned based on the stacking sequence of the laminate. A three-dimensional mesh of 43,200 eight-node full-integration hexahedral elements was used for each ply. The temperature change ΔT was applied to the analysis model to reproduce the thermal residual strains due to the temperature difference between the fabrication temperature and room temperature. Then, incremental uniaxial displacement was applied to the edge of the analysis model with a displacement rate of 0.5 mm/min and a time increment of 0.96 s. A static explicit FE code employing the direct sparse solver PARDISO provided by the Intel Math Kernel Library (ASTM International, 2012) was developed and used for the mesoscopic analysis.

2.2. Microscopic periodic unit cell analysis

To predict the crack initiation under several loading conditions, a three-dimensional unit cell model comprising five carbon fibers and a polymer matrix was developed. Fig. 4 shows the mesh of the FE model used for the microscopic analysis along with the applied periodic boundary conditions (PBCs). The carbon fibers were modeled as an orthotropic elastic body whereas the mechanical behavior of the matrix was described by an isotropic elasto-viscoplastic formulation. In this study, the fiber and the matrix were assumed to be perfectly bonded in order to focus only on the matrix cracking. Further, PBCs were imposed on the unit cell model (Fig. 4). A three-dimensional mesh of approximately 55,000 ten-node second-order tetrahedral elements was used for the unit cell. A static-explicit FE code employing the direct sparse solver PARDISO (ASTM International, 2012) was developed and used for the microscopic PUC analysis.

To predict the initiation of matrix cracking, nonlinear material behavior was considered in the matrix phase in the PUC analysis. The nonlinear stress–strain response of the epoxy resin was reproduced by the following an elasto-viscoplastic model:

$$\dot{\boldsymbol{\sigma}} = \mathbf{C}_{\mathrm{m}}^{\mathrm{e}} : \dot{\boldsymbol{\varepsilon}} - \frac{3\mu\dot{\bar{\varepsilon}}^{\mathrm{p}}}{\bar{\sigma}}\boldsymbol{\sigma}' \tag{4}$$

where $\boldsymbol{\sigma}$ is the stress tensor, $\mathbf{C}_{\mathrm{m}}^{\mathrm{e}}$ is the elastic stiffness tensor for the matrix resin, $\boldsymbol{\varepsilon}$ is the strain tensor, μ is the Lamé constant, $\bar{\varepsilon}^{\mathrm{p}}$

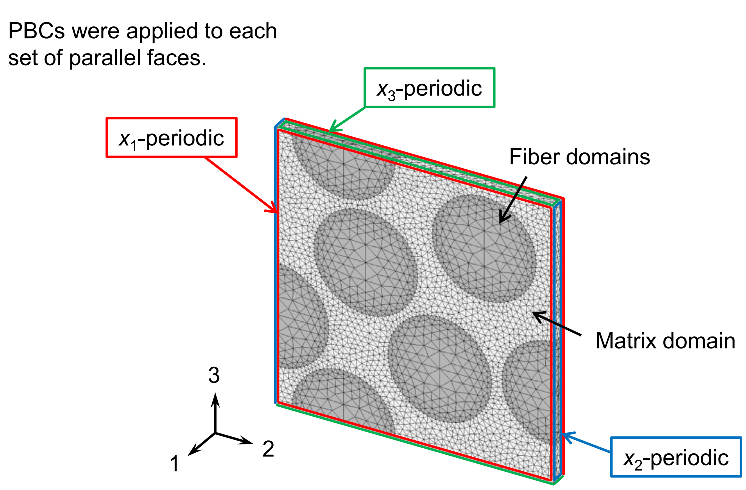

Fig. 4. FE model for microscopic PUC analysis.

Table 2
Material properties of matrix resin used in PUC analysis.

Reference strain rate $\dot{\varepsilon}_r$	1.0×10^{-5}
Strain-rate sensitivity parameter m	1/35
Hydrostatic stress sensitivity β	0.2
Hardening rule g_1	90 MPa
g_2	0.08
g_3	20 MPa
Tensile strength of resin T	120 MPa
Compressive strength of resin C	200 MPa
Dimensionality for nonlocalization k	3
Reference length for nonlocalization l	0.15 µm

is the equivalent plastic strain, $\bar{\sigma}$ represents the von Mises stress, $\boldsymbol{\sigma}'$ the deviatoric stress tensor, and $\cdot$ indicates time differentiation. Following Matsuda et al. (2002), the equivalent plastic strain rate $\dot{\bar{\varepsilon}}^{\mathrm{p}}$ was determined leveraging the following equations, including the hydrostatic stress dependence (Okabe et al., 2011):

$$\dot{\bar{\varepsilon}}^{\mathrm{p}} = \dot{\varepsilon}_{\mathrm{r}} \left(\frac{\bar{\sigma} + \beta\sigma_{\mathrm{m}}}{g(\bar{\varepsilon}^{\mathrm{p}})} \right)^{\frac{1}{m}}, \tag{5}$$

$$g(\bar{\varepsilon}^{\mathrm{p}}) = g_1 (\bar{\varepsilon}^{\mathrm{p}})^{g_2} + g_3. \tag{6}$$

Here, $\dot{\varepsilon}_{\mathrm{r}}$ is the reference strain rate; σ_{m} is hydrostatic stress; m is an exponent controlling the strain rate sensitivity; β defines the hydrostatic stress sensitivity; and g_1, g_2 and g_3 are material constants. We assumed $\dot{\varepsilon}_{\mathrm{r}} = 1.0 \times 10^{-5}$, $m = 1/35$, $\beta = 0.2$, in accordance with a previous report (Okabe et al., 2011). The values $g_1 = 90$ MPa, $g_2 = 0.08$, and $g_3 = 20$ MPa were determined based on the neat resin experiment performed by Fiedler et al. (2001).

The process of matrix crack onset was predicted by Christensen's failure criterion (Christensen, 2013), which account for both brittle failure under elastic deformation and ductile failure under plastic deformation:

$$F = 3\left(1 - \frac{T}{C}\right)\hat{\sigma}_{\mathrm{m}} + \hat{\bar{\sigma}}^2 \le \frac{T}{C} \tag{7}$$

Here, T and C are the tensile and compressive strength of the resin, and $\hat{\sigma}_{\mathrm{m}}$ and $\hat{\bar{\sigma}}$ are the hydrostatic and equivalent stresses normalized by C, respectively. In this study, we assumed $T = 120$ MPa and $C = 200$ MPa, as proposed in Kumagai et al. (2017). To avoid spurious mesh dependence in the presence of matrix damage, nonlocalization of the variable F was conducted according to literature (Bažant and Pijaudier-Cabot, 1988):

$$\bar{F}(\boldsymbol{x}) = \frac{1}{V_{\mathrm{r}}(\boldsymbol{x})} \int_V h(\boldsymbol{s} - \boldsymbol{x}) F(\boldsymbol{s}) \mathrm{d}V(\boldsymbol{s}), \tag{8}$$

$$h(\boldsymbol{x}) = \exp\left\{ -\frac{k|\boldsymbol{x}|^2}{l^2} \right\}, \tag{9}$$

$$V_{\mathrm{r}}(\boldsymbol{x}) = \int_V h(\boldsymbol{s} - \boldsymbol{x}) \mathrm{d}V(\boldsymbol{s}). \tag{10}$$

Here, $\bar{F}$ is the nonlocalized damage parameter, V is the reference volume, k is the dimensionality ($k = 3$ in this study), and l is a reference length for nonlocalization. We considered that $l = 0.15$ µm, as reported previously (Okabe et al., 2011).

The material properties used in the PUC analysis are listed in Table 2.

Finally, the FE formulation for PUC analysis is briefly explained. The fiber region, the matrix region, and the mechanical boundary are expressed by V_{f}, V_{m}, and S_{t}, respectively. The principle of virtual work is written as,

$$\int_{V_{\mathrm{f}}} \boldsymbol{\sigma} : \delta\boldsymbol{\varepsilon} \mathrm{d}V + \int_{V_{\mathrm{m}}} \boldsymbol{\sigma} : \delta\boldsymbol{\varepsilon} \mathrm{d}V = \int_{S_{\mathrm{t}}} \boldsymbol{f} \cdot \delta\boldsymbol{u} \mathrm{d}S. \tag{11}$$

Here, $\boldsymbol{f}$ is the external force vector acting on S_{t}, $\boldsymbol{u}$ is the displacement vector, and δ represents the virtual component. Now we employ quasi-static formulation to solve unknown states at time $t' = t + \Delta t$ using known physical quantities at time t. The linearization of Eq. (11) assuming the limit $\Delta t \to 0$ gives the following equation:

$$\begin{aligned} \Delta t & \left(\int_{V_{\mathrm{f}}} {}^t\dot{\boldsymbol{\sigma}} : \delta\boldsymbol{\varepsilon} \mathrm{d}V + \int_{V_{\mathrm{m}}} {}^t\dot{\boldsymbol{\sigma}} : \delta\boldsymbol{\varepsilon} \mathrm{d}V \right) \\ & = \int_{S_{\mathrm{t}}} {}^{t'}\boldsymbol{f} \cdot \delta\boldsymbol{u} \mathrm{d}S - \left(\int_{V_{\mathrm{f}}} {}^t\boldsymbol{\sigma} : \delta\boldsymbol{\varepsilon} \mathrm{d}V + \int_{V_{\mathrm{m}}} {}^t\boldsymbol{\sigma} : \delta\boldsymbol{\varepsilon} \mathrm{d}V \right). \end{aligned} \tag{12}$$

The constitutive law for a fiber is given by

$$\dot{\boldsymbol{\sigma}} = \boldsymbol{C}_{\mathrm{f}}^{\mathrm{e}} : \dot{\boldsymbol{\varepsilon}}. \tag{13}$$

Here, $\boldsymbol{C}_{\mathrm{f}}^{\mathrm{e}}$ is the elastic stiffness tensor of the fiber. Substituting Eqs. (4) and (13) into Eq. (12) gives the following virtual work equation:

$$\begin{aligned} & \int_{V_{\mathrm{f}}} \left(\boldsymbol{C}_{\mathrm{f}}^{\mathrm{e}} : \Delta\boldsymbol{\varepsilon} \right) : \delta\boldsymbol{\varepsilon} \mathrm{d}V + \int_{V_{\mathrm{m}}} \left(\boldsymbol{C}_{\mathrm{m}}^{\mathrm{e}} : \Delta\boldsymbol{\varepsilon} \right) : \delta\boldsymbol{\varepsilon} \mathrm{d}V \\ & \quad = \int_{S_{\mathrm{t}}}^{t'} \boldsymbol{f} \cdot \delta\boldsymbol{u} \mathrm{d}S - \int_{V_{\mathrm{f}}+V_{\mathrm{m}}}^{t} \boldsymbol{\sigma} : \delta\boldsymbol{\varepsilon} \mathrm{d}V \\ & \quad + \int_{V_{\mathrm{m}}} \frac{3\mu\Delta\bar{\varepsilon}^{\mathrm{p}}}{\bar{\sigma}} \left(\boldsymbol{\sigma}_t{}' : \delta\boldsymbol{\varepsilon} \right) \mathrm{d}V. \end{aligned} \tag{14}$$

In the PUC analysis, the displacement vector $\boldsymbol{u}$ and the strain increment $\Delta\boldsymbol{\varepsilon}$ should be decomposed into a global component that represents the average deformation of a unit cell and a local component that corresponds to a local deviation in the unit cell.

$$\begin{aligned} \boldsymbol{u} & = \boldsymbol{u}_{\mathrm{G}} + \boldsymbol{u}_{\mathrm{L}} \\ \Delta\boldsymbol{\varepsilon} & = \Delta\boldsymbol{\varepsilon}_{\mathrm{G}} + \Delta\boldsymbol{\varepsilon}_{\mathrm{L}} \end{aligned} \tag{15}$$

Here, the subscripts G and L represent the global component and local component, respectively. The global component is a constant regardless of the local coordinate system in the unit cell. Applying this decomposition to Eq. (14), the following equation is derived:

$$\begin{aligned} & \int_{V_{\mathrm{f}}} \left(\boldsymbol{C}_{\mathrm{f}}^{\mathrm{e}} : \Delta\boldsymbol{\varepsilon}_{\mathrm{L}} \right) : \delta\boldsymbol{\varepsilon} \mathrm{d}V + \int_{V_{\mathrm{m}}} \left(\boldsymbol{C}_{\mathrm{m}}^{\mathrm{e}} : \Delta\boldsymbol{\varepsilon}_{\mathrm{L}} \right) : \delta\boldsymbol{\varepsilon} \mathrm{d}V \\ & = -\int_{V_{\mathrm{f}}+V_{\mathrm{m}}} {}^t\boldsymbol{\sigma} : \delta\boldsymbol{\varepsilon} \mathrm{d}V + \int_{V_{\mathrm{m}}} \frac{3\mu\Delta\bar{\varepsilon}^{\mathrm{p}}}{\bar{\sigma}} \left({}^t\boldsymbol{\sigma}' : \delta\boldsymbol{\varepsilon} \right) \mathrm{d}V \\ & \quad - \int_{V_{\mathrm{f}}} \left(\boldsymbol{C}_{\mathrm{f}}^{\mathrm{e}} : \Delta\boldsymbol{\varepsilon}_{\mathrm{G}} \right) : \delta\boldsymbol{\varepsilon} \mathrm{d}V - \int_{V_{\mathrm{m}}} \left(\boldsymbol{C}_{\mathrm{m}}^{\mathrm{e}} : \Delta\boldsymbol{\varepsilon}_{\mathrm{G}} \right) : \delta\boldsymbol{\varepsilon} \mathrm{d}V. \end{aligned} \tag{16}$$

In Eq. (16), the mechanical boundary S_{t} disappears because of the periodic boundary condition. Finally, discretization of Eq. (16) gives the following simultaneous linear equation:

$$\left({}^t\boldsymbol{K}_{\mathrm{f}} + {}^t\boldsymbol{K}_{\mathrm{m}} \right) \Delta\boldsymbol{U}_{\mathrm{L}} = -\left({}^t\boldsymbol{Q}_{\mathrm{f}} + {}^t\boldsymbol{Q}_{\mathrm{m}} \right) + {}^t\boldsymbol{Q}_{\mathrm{v}} - \left(\Delta\boldsymbol{Q}_{\mathrm{f,G}} + \Delta\boldsymbol{Q}_{\mathrm{m,G}} \right) \tag{17}$$

where

$$\begin{aligned} \boldsymbol{K}_{\mathrm{f}} & = \sum_{\mathrm{e}} \int_{V_{\mathrm{f}}^{\mathrm{e}}} \boldsymbol{B}^{\mathrm{eT}} \boldsymbol{D}_{\mathrm{f}}^{\mathrm{e}} \boldsymbol{B}^{\mathrm{e}} \mathrm{d}V, \quad \boldsymbol{K}_{\mathrm{m}} = \sum_{\mathrm{e}} \int_{V_{\mathrm{m}}^{\mathrm{e}}} \boldsymbol{B}^{\mathrm{eT}} \boldsymbol{D}_{\mathrm{m}}^{\mathrm{e}} \boldsymbol{B}^{\mathrm{e}} \mathrm{d}V, \\ \boldsymbol{Q}_{\mathrm{f}} & = \sum_{\mathrm{e}} \int_{V_{\mathrm{f}}^{\mathrm{e}}} \boldsymbol{B}^{\mathrm{eT}} \hat{\boldsymbol{\sigma}} \mathrm{d}V, \quad \boldsymbol{Q}_{\mathrm{m}} = \sum_{\mathrm{e}} \int_{V_{\mathrm{m}}^{\mathrm{e}}} \boldsymbol{B}^{\mathrm{eT}} \hat{\boldsymbol{\sigma}} \mathrm{d}V, \\ \boldsymbol{Q}_{\mathrm{v}} & = \sum_{\mathrm{e}} \int_{V_{\mathrm{m}}^{\mathrm{e}}} \frac{3\mu\Delta\bar{\varepsilon}^{\mathrm{p}}}{\bar{\sigma}} \boldsymbol{B}^{\mathrm{eT}} \hat{\boldsymbol{\sigma}}' \mathrm{d}V, \\ \Delta\boldsymbol{Q}_{\mathrm{f,G}} & = \sum_{\mathrm{e}} \int_{V_{\mathrm{f}}^{\mathrm{e}}} \boldsymbol{B}^{\mathrm{eT}} \boldsymbol{D}_{\mathrm{f}}^{\mathrm{e}} \Delta\boldsymbol{\varepsilon}_{\mathrm{G}} \mathrm{d}V, \quad \Delta\boldsymbol{Q}_{\mathrm{m,G}} = \sum_{\mathrm{e}} \int_{V_{\mathrm{m}}^{\mathrm{e}}} \boldsymbol{B}^{\mathrm{eT}} \boldsymbol{D}_{\mathrm{m}}^{\mathrm{e}} \Delta\boldsymbol{\varepsilon}_{\mathrm{G}} \mathrm{d}V. \end{aligned} \tag{18}$$

Here, $\Delta\boldsymbol{U}$ is the nodal displacement increment, $\boldsymbol{K}_{\mathrm{f}}$ is the stiffness matrix of the fiber elements, $\boldsymbol{K}_{\mathrm{m}}$ is the stiffness matrix of the matrix elements, $\boldsymbol{Q}$ is the internal force vector, $\boldsymbol{Q}_{\mathrm{v}}$ is the internal force

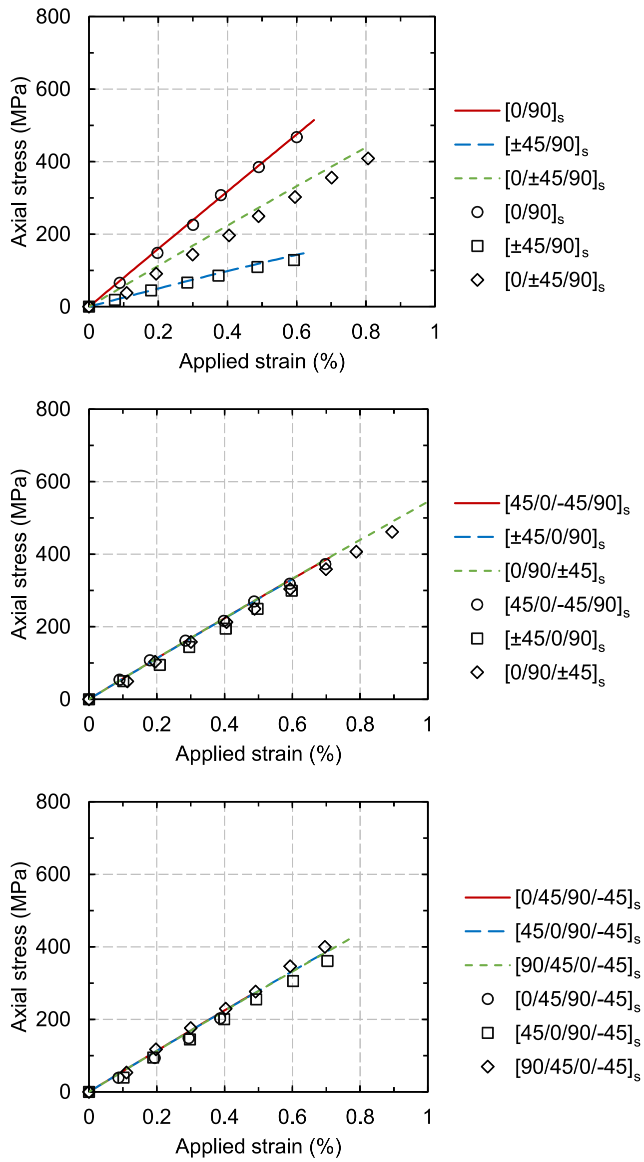

Fig. 5. Comparison of stress–strain curves obtained by mesoscopic laminate analysis and experiments (experimental data up to first transverse cracking taken from Kobayashi et al. (2000) and Ogihara et al. (2001)).

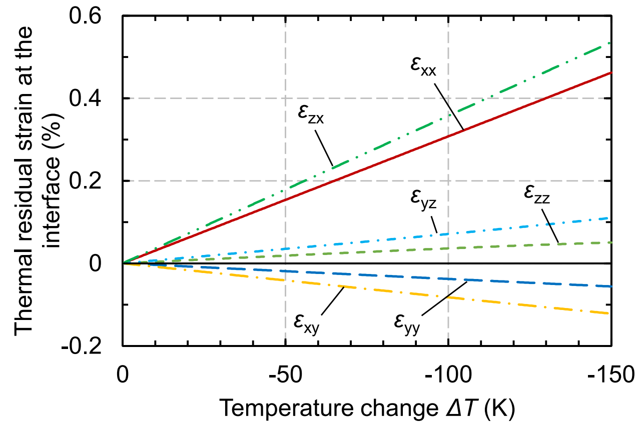

(a) Strain histories during thermal analysis

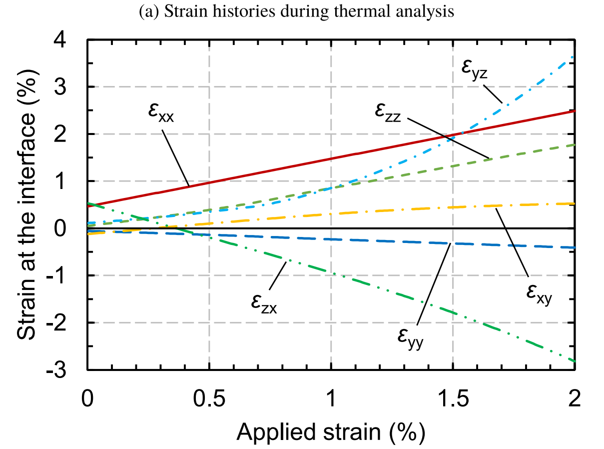

(b) Strain histories during tensile loading after thermal analysis with $\Delta T = 150$ K

Fig. 6. Strain histories of the 90° layer at the −45°/90° interface of the $[0/\pm45/90]_s$ laminate obtained by mesoscopic analysis: (a) strain against temperature change and (b) strain against applied macroscopic axial strain.

vector derived from viscous components in Eq. (4), $\boldsymbol{B}$ is the compatibility matrix between the strain and displacement, $\boldsymbol{D}$ is the constitutive matrix, and $\hat{\boldsymbol{\sigma}}$ is a vector form of the stress tensor. $\boldsymbol{Q}_{\mathrm{f,G}}$ and $\boldsymbol{Q}_{\mathrm{m,G}}$ are the internal force vectors driven by the macroscopic strain increment $\Delta\boldsymbol{\varepsilon}_{\mathrm{G}}$. The PUC analysis was conducted based on the macroscopic strain increment $\Delta\boldsymbol{\varepsilon}_{\mathrm{G}}$ that was determined from mesoscopic analysis described in Section 2.1.

2.3. Computational procedure

To account for the microscopic structure of composites and their macroscopic deformation simultaneously, the multiscale analysis described in the previous sections was carried out. The approach can be summarized as follows.

(1) The thermal residual strain for each location in the laminate was calculated by the macroscopic 3D FEA, for the curing temperature down to room temperature. After calculating the thermal residual strain, incremental external displacement was applied to the FE model. During the analysis, the strain history at the locations of expected crack initiation in the laminate was stored at each step.
(2) The thermal stresses in the unit cell model were calculated, decreasing the temperature from the curing to room temperature. Here, the incremental global strain was adjusted by a simple feedback approach so that the global stress components were zero (Okabe et al., 2015). The stress/strain field obtained from this calculation was assumed as the initial state.
(3) The strain history obtained in step (1) was applied as the global strain increment of the microscopic 3D PUC model. The initial cracking strain was defined as the applied strain of the laminate at which the failure criterion described in the previous section was first satisfied for an element.

3. Multiscale analysis of tensile tests on quasi-isotropic and cross-ply laminates of T800H/3900-2

Multiscale crack prediction was conducted for experimental data available in literature to demonstrate the crack prediction capability. The following subsections describe the simulation settings of the multiscale analysis and discuss the results.

3.1. Problem description

Our multiscale analysis was applied to the tensile tests on quasi-isotropic and cross-ply laminates conducted by

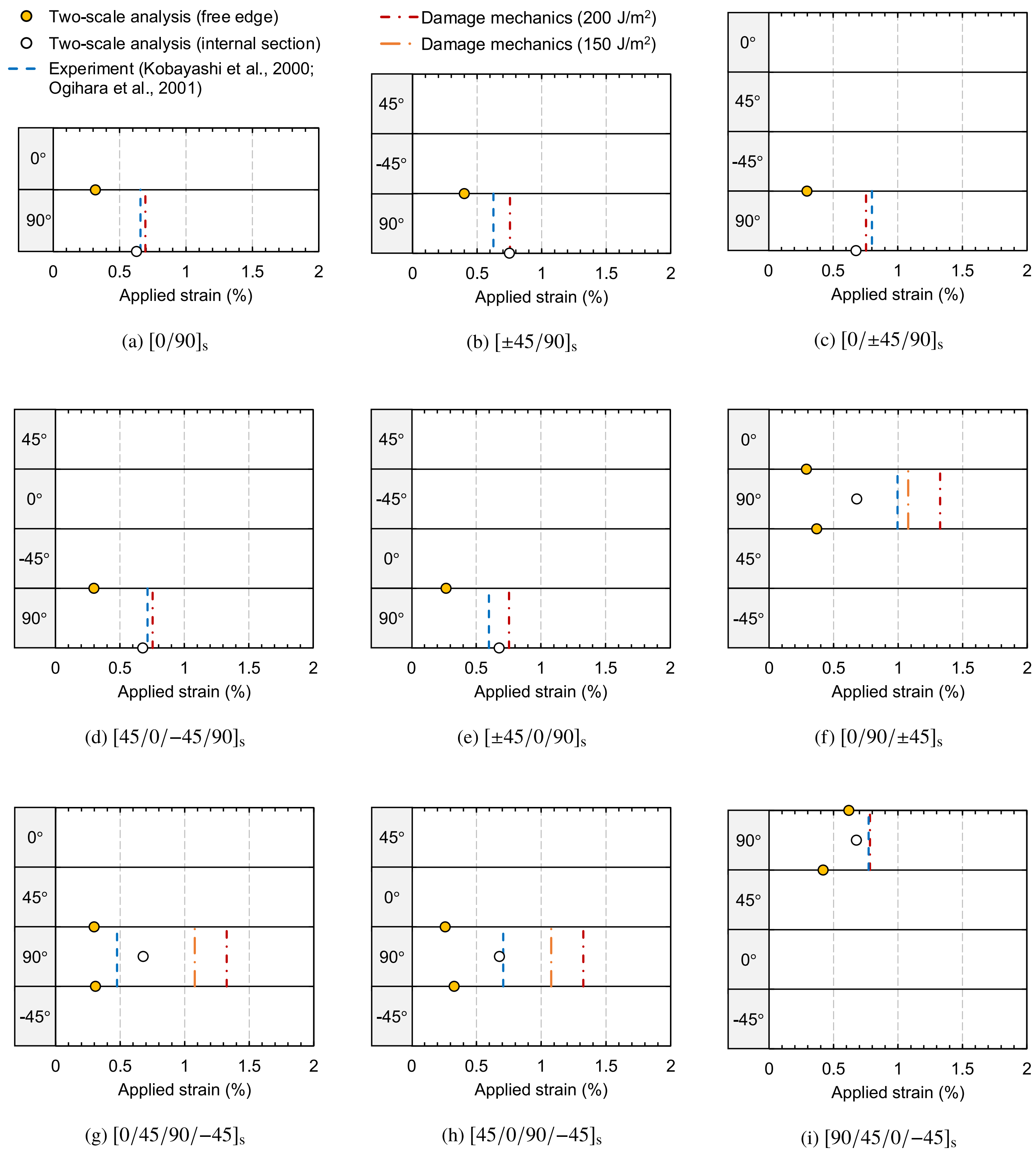

Fig. 7. Comparison of predicted initial cracking strains with experimental results. The blue dashed lines show experimentally characterized strains of transverse crack initiation (Kobayashi et al., 2000; Ogihara et al., 2001). Results of simulations are represented by solid symbols. (For interpretation of the references to color in this figure legend, the reader is referred to the web version of this article.)

Kobayashi et al. (2000) and Ogihara et al. (2001). In the experiments, tensile loading was interrupted at certain strain levels, and then the number of transverse cracks was counted using optical microscopy and soft X-ray tomography. The transverse crack was defined as a crack that completely propagated over the width of the laminate. In our analysis, the first transverse cracks in the 90° ply were predicted for nine laminate configurations listed in Table 3. Because of the symmetrical stacking sequence of the laminates, only half of the laminate was discretized for the mesoscopic FE analysis, as shown in Fig. 3. Expected cracking points on the mesoscopic analysis were determined based on the experimental and computational studies of the initial cracks in

Table 3
Laminate configurations and specimen dimensions used for multiscale analysis of T800H/3900-2 laminated composites.

Laminate configuration	Gauge length (mm)	Width (mm)	Ply thickness (mm)
$[0/90]_s$ $[\pm 45/90]_s$ $[0/\pm 45/90]_s$ $[45/0/-45/90]_s$ $[\pm 45/0/90]_s$ $[0/90/\pm 45]_s$ $[0/45/90/-45]_s$ $[45/0/90/-45]_s$ $[90/45/0/-45]_s$	80	25	0.18

cross-ply laminates reported by Okabe et al. (2015). According to their work, the first crack in the 90° ply of cross-ply laminates was initiated at the free-edge interlaminar area. Subsequently, the cracks are generated on the midplane of the 90° ply. Based on the results, strain histories used for subsequent PUC analysis were extracted from the free-edge interlaminar area between 90° and neighboring plies and from the center of the thickness and width of the 90° ply. The longitudinal positions for both strain-extracted points were at the center of the length of the model, i.e. $x = L/2$. Material constants used for mesoscopic and microscopic FE analyses are summarized in Table 4. These material constants were collected from literature (Shigemori et al., 2014; Toray Composite Materials America, 2018b; Yoshioka et al., 2016) to avoid material property fitting. Consistency between mesoscopic analysis and microscopic PUC analysis was discussed in Appendix A.

3.2. Results and discussion

First, the mesoscale FE analysis was performed to obtain the strain data for the subsequent microscopic analysis. Fig. 5 compares the stress–strain curves obtained by our mesoscopic FE analysis to the experimental data reported by Kobayashi et al. (2000) and Ogihara et al. (2001). Solid and dashed lines show our predictions whereas the symbols represent the experimental data up to the transverse crack initiation. As can be noted, our mesoscopic analysis, based on the anisotropic elasto-plastic constitutive model described by Eqs. (1)–(3), successfully reproduced the stress–strain response up to failure initiation for every laminate configuration investigated in this work. On the other hand, Fig. 6(a) and (b) show the strain histories obtained from the 90° layer at the −45°/90° interface of the $[0/\pm 45/90]_s$ laminate. In Fig. 6(a), the mesoscale strain components are plotted as a function of the temperature change from curing temperature to room temperature and, in Fig. 6(b), the strain components are plotted against the applied macroscopic uniaxial strain. These non-trivial strains were applied to the unit cell used in the microscopic analysis to predict the strains at the onset of the first cracks in the 90° layer of the laminated composites.

After imposing the macroscopic strain to the PUC, the microscopic model was solved by FEA to calculate the related stress distribution in the matrix according to the elasto-viscoplastic model described by Eqs. (4)–(6). Then, employing Christensen's failure criterion (Christensen, 2013) in the form summarized by Eq. (7), initiation of the first matrix cracks could be identified for the 90° layer. Figs. 7(a)–(i) summarize the comparison between the simulated initial cracking strains obtained by our multiscale analysis and suggested by the experimental values as reported in literature (Kobayashi et al., 2000; Ogihara et al., 2001). In each figure, the horizontal axes indicate the mesoscopic strain applied to the laminates, calculated by subtracting the thermal residual strain from the total strain of the unit cell, whereas the vertical axes schematically represent the locations in the laminate investigated in the PUC analysis. Colored and uncolored plots represent the simulated results obtained from free edges and internal sections respectively, whereas the experimental results by Kobayashi et al. (2000) and Ogihara et al. (2001) are represented in the figure by blue dashed lines. In all cases, the first crack of the ply initiated at the interlaminar area of the ply on the free edge, followed by a crack at the internal section. This implies that an initial microcrack occurs at the interlaminar on the free edge, and then grows to a transverse crack. As seen in Fig. 7(a)–(i), internal cracks obtained by FE analysis agreed well with experimental initial transverse cracking strains except for the $[0/90/\pm 45]_s$ laminate. To understand the transverse crack initiation of the 90° ply in further detail, cracking strains of the laminates were predicted by the following energy-based criterion, and compared with the multiscale analysis and experimental results:

$$\Gamma(\rho) > \Gamma_c, \tag{19}$$

$$\Gamma(\rho) = -\frac{U(\rho/2) - 2U(\rho)}{t}, \tag{20}$$

where Γ_c is the critical energy release rate, U is the strain energy of the laminate, t is the ply thickness, and ρ is the ply crack density. The critical energy release rate $\Gamma_c = 200$ J/m^2 was determined through comparison of predicted and experimental values of the $[0/90]_s$ laminate. Details on the energy-based criterion can be found in Appendix B. The predicted cracking strains of the energy criterion are shown in Fig. 7 by red dashed dotted lines. As seen in Fig. 7(a)–(e) and (i), the predicted values of the energy criterion agreed well with the numerical and experimental results. On the other hand, the energy criterion overestimated the cracking strains, as shown in Fig. 7(f)–(h). For these cases, predicted values with $\Gamma_c = 150$ J/m^2 are also shown in the figures by orange dashed dotted lines. In the case of Fig. 7(f), the predicted value with $\Gamma_c = 150$ J/m^2 agreed well with experimental one, which is the case that the multiscale simulation underestimated the value. This can be explained based on the multiscale prediction that the critical energy release rate is decreased by the failure process zone near the crack tip generated at the early loading stage. As seen in Fig. 7(g) and (h), the energy criterion with $\Gamma_c = 150$ J/m^2 still overestimated the experimental transverse cracking strain. In these cases, the neighboring plies of the 90° layer had different fiber angles, e.g. 45° and −45°. The energy criterion assumed both ply interfaces to have been deformed uniformly determined by the applied strain and thus did not account for nonuniform deformation due to different angles of neighboring plies. This discrepancy can be one of the reasons for the overestimation of the energy criterion as seen in Fig. 7(g) and (h).

As can be noted in Fig. 7(a)–(i), in all of the 90° layers, the first crack initiated near the interlaminar area on the free edge of the laminate. Subsequent cracks occurred at the internal section of the plies. Fig. 8 shows the stress–strain curves obtained by the PUC analysis of the 90° ply of the $[0/45/90/-45]_s$ laminate. In this figure, the axial stress is the volume-averaged stress over the unit cell whereas the strain in the x-axis represents the mesoscale axial strain composed of strains due to both thermal and mechanical loadings. The open circles correspond to the cracking strains presented in Fig. 7(g). In the free-edge cases, the axial stress was higher than that of the internal case, and the cracking strain was smaller than that of the internal one. This is because a multiaxial stress state was induced near the free edge by the interaction between the 90° and neighboring plies. Figs. 9 and 10 present the hydrostatic stress, equivalent stress, and matrix crack distribution obtained by PUC analysis of the $[0/45/90/-45]_s$ laminate at each loading step. In the stress distribution, only the matrix elements are visualized for clarity. In the matrix crack initiation patterns, the fiber and cracked matrix elements are plotted by blue and red elements, respectively. Based on comparison of Figs. 9(a) and 10(a),

Table 4
Mechanical properties used in mesoscopic FE analysis and PUC analysis of T800H/3900-2 laminates

Mesoscopic FE analysis[a]	
Longitudinal Young's modulus E_1	151 GPa
Transverse Young's modulus E_2, E_3	9.16 GPa
Shear modulus G_{12}, G_{13}	4.62 GPa
Shear modulus G_{23}	2.55 GPa
Poisson's ratio ν_{12}, ν_{13}	0.302
Poisson's ratio ν_{23}	0.589
Coefficient of thermal expansion for longitudinal direction α_1	0×10^{-6}/K
Coefficient of thermal expansion for transverse direction α_2, α_3	33×10^{-6}/K
Temperature change ΔT	−150 K
Microscopic PUC analysis	
Fiber longitudinal Young's modulus E_L	294 GPa[b]
Fiber transverse Young's modulus E_T	19.5 GPa[c]
Fiber longitudinal Poisson's ratio ν_L	0.17[c]
Fiber transverse Poisson's ratio ν_T	0.46[c]
Fiber's coefficient of thermal expansion for longitudinal direction α_L	-1.1×10^{-6}/K[c]
Fiber's coefficient of thermal expansion for transverse direction α_T	10×10^{-6}/K[c]
Matrix Young's modulus E_m	3.2 GPa[c]
Matrix Poisson's ratio ν_m	0.38[c]
Matrix's coefficient of thermal expansion α_m	60×10^{-6}/K[c]
Fiber volume fraction V_f	56%
Fiber diameter d_f	5 μm[b]

[a] All mechanical properties for mesoscopic analysis were taken from Shigemori et al. (2014).
[b] Properties were taken from Datasheet (Toray Composite Materials America, 2018b).
[c] Properties were taken from Yoshioka et al. (2016).

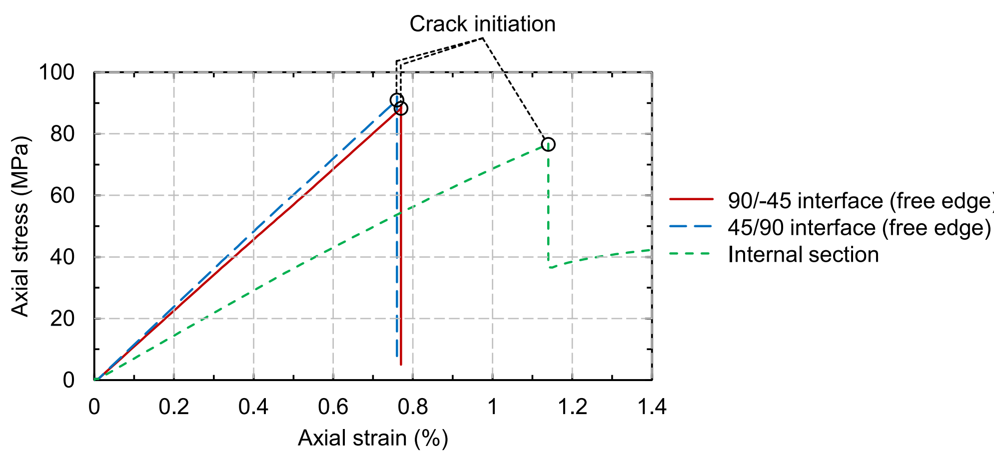

Fig. 8. Comparison of stress–strain curves obtained by PUC analysis of $[0/45/90/-45]_s$ laminates.

the hydrostatic stress at the free edge was higher than that at the internal section due to the free-edge effect. As shown in Fig. 9(b), this higher hydrostatic stress induced crack initiation at the inter-fiber matrix where fibers were aligned parallel to the loading direction. In the case of the internal section, the matrix crack initiated at the inter-fiber matrix at a higher axial strain because of the lower hydrostatic stress concentration than in the case of the free edge, as indicated in Fig. 10(b). This cracking sequence in the 90° ply was consistent with the experimental and numerical results reported for cross-ply laminates by Okabe et al. (2015). These results indicate that the dominant crack formation mechanism of the 90° ply in cross-ply and quasi-isotropic laminates is identical.

Next, to investigate the initial cracking on the 90° ply in quasi-isotropic laminates in further detail, detailed microscopic observation of crack initiation and multiscale analysis were conducted.

4. Experimental observation and multiscale analysis of tensile tests on quasi-isotropic and cross-ply laminates of T700S/2592

Experimental observation of microcracking and multiscale analysis were undertaken to investigate the onset of matrix cracking on the 90° ply in quasi-isotropic laminates in greater detail. The experiment procedure, simulation conditions, and experimental and simulated results are presented in the following subsections.

4.1. Experiments

Tensile tests on laminated composites were performed following procedures reported in the literature (Kobayashi et al., 2000; Ogihara et al., 2001) with a different material system to validate our multiscale approach. Laminate configurations and specimen dimensions used for the experiment are presented in Table 5.

Laminate specimens were made from unidirectional prepreg sheets of T700S/2592 (Toray Industries). The prepreg sheets were stacked with the laminate configuration shown in Table 5. The laminated sheets were then cured in an autoclave (ASHIDA MFG Co.) under a gauge pressure of 0.3 MPa and a holding temperature of 130 °C for 2 h. Cured laminates were cut into specimens with the dimensions specified in Table 5. Unidirectional laminates were used for elastic modulus measurements, and cross-ply and quasi-isotropic laminates were employed for initial crack observation.

For tensile testing, GFRP tabs with a thickness of 1.5 mm were bonded on a specimen. Monotonic tensile loading with a displacement rate of 0.5 mm/min was applied to a specimen by a servohy-

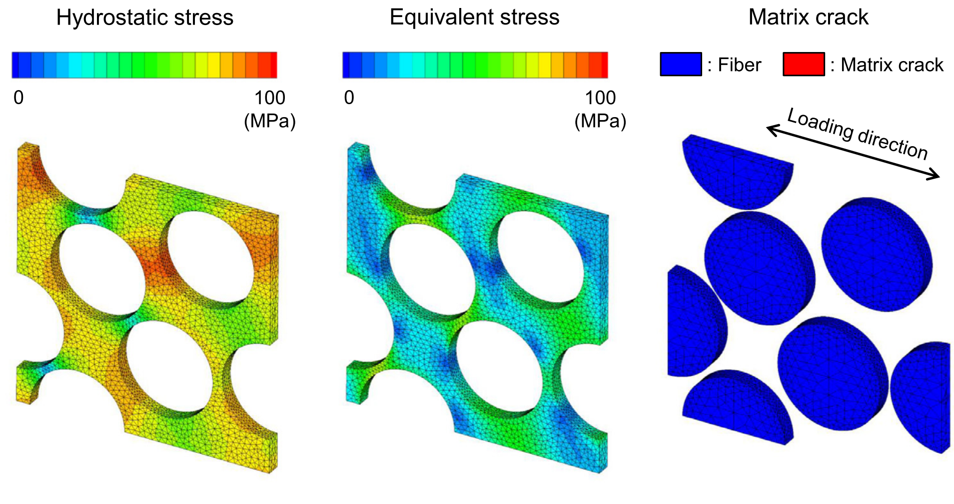

(a) Before crack initiation (axial strain = 0.60%)

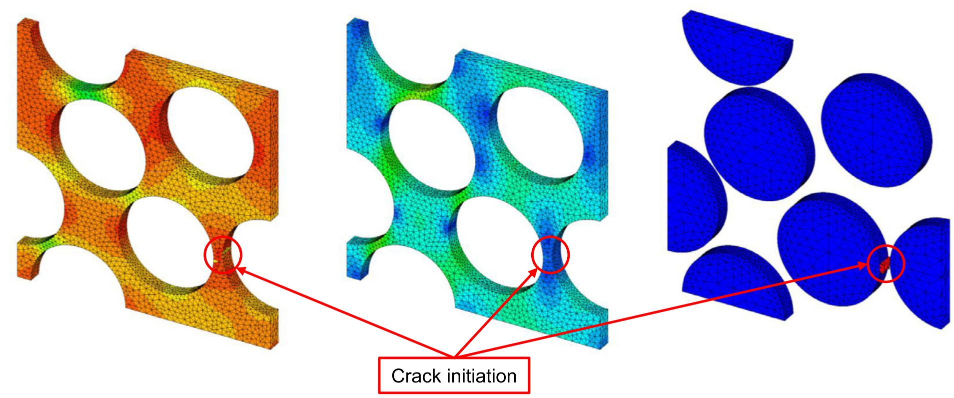

(b) Right after crack initiation (axial strain = 0.76%)

Fig. 9. Hydrostatic stress, equivalent stress, and matrix crack distribution obtained by PUC analysis at 45/90 interface on free edge of 90° ply of $[0/45/90/-45]_s$ laminate at each loading step.

Table 5
Laminate configurations and specimen dimensions used for experiments and multiscale analysis of T700S/2592 laminates.

Laminate configuration	Length (mm)	Width (mm)	Ply thickness (mm)	End-tab size (mm)
$[0]_8$	250	15	0.10	56 × 15
$[90]_{16}$				25 × 15
$[45]_{16}$				25 × 15
$[0/90]_s$	150	25	0.10	35 × 25
$[\pm 45/0/90]_s$				
$[0/90/\pm 45]_s$				
$[0/45/90/-45]_s$				

draulic testing machine (MTS Systems Corporation), and specimen deformation was measured by strain gauges (Kyowa Electronic Instruments Co.) attached on the laminate. An edge face of cross-ply and quasi-isotropic laminates was polished to observe transverse cracks by the replication technique (International, 2012). For the replication technique, the tensile loading was interrupted at intervals of 0.1% strain, and a replica of a specimen edge face was obtained using RepliSet (Struers), as shown in Fig. 11. After an initial transverse crack was observed by microscopy on the replica films, X-ray computed tomography was conducted to confirm that generated cracks propagated over the width of a specimen.

4.2. Simulation conditions

In the multiscale analysis, the first transverse cracks in the 90° ply were predicted for cross-ply and quasi-isotropic laminates as listed in Table 5. In the same way as in the case of T800H/2900-2, only half of the laminate was discretized for the mesoscopic FE analysis because of the symmetrical configuration of the laminates. Mechanical properties used for mesoscopic and microscopic FE analyses are presented in Table 6. Mechanical properties for mesoscopic analysis were determined from tensile tests of unidirectional laminates listed in Table 5 and the other properties were taken from literature (Okabe et al., 2015; Toray Composite Materials America, 2018a). In the next subsection, the simulated results of the two-scale analysis are compared to the experimental results to confirm the dominant crack formation mechanism on the 90° ply in quasi-isotropic laminates.

4.3. Results and discussion

Fig. 12 summarizes the experimental and simulated results obtained by our experiment and multiscale FE analysis. In each figure, colored and uncolored symbols represent the simulated results obtained for free edges and internal sections, respectively. The ranges of experimental initial and transverse cracking strains on the free edge are denoted by red and blue rectangles, respectively. The predicted cracking strains of the energy criterion are also shown in

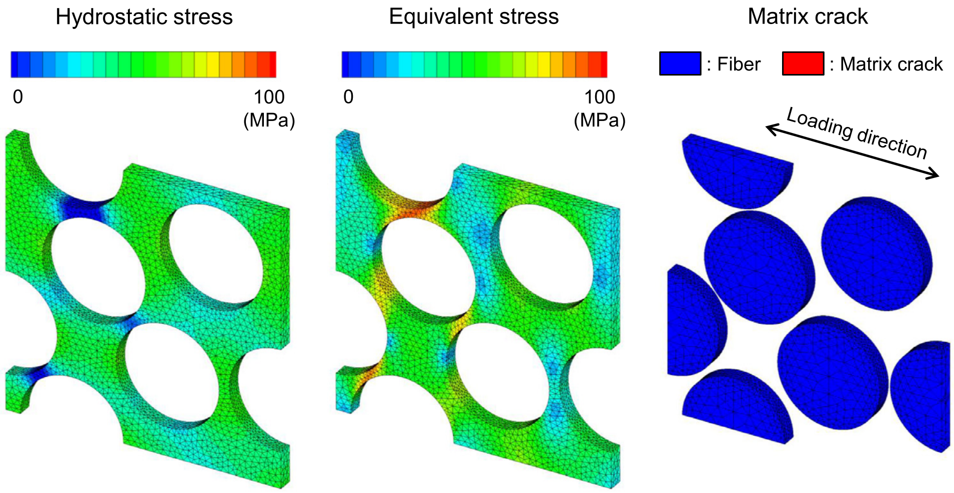

(a) Before crack initiation (axial strain = 0.60%)

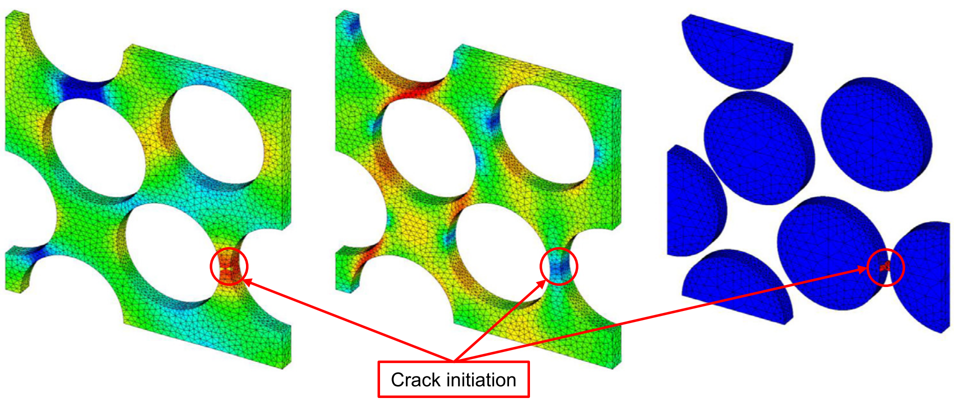

(b) Right after crack initiation (axial strain = 1.14%)

Fig. 10. Hydrostatic stress, equivalent stress, and matrix crack distribution obtained by PUC analysis at center of ply thickness on internal section of 90° ply of $[0/45/90/-45]_s$ laminate at each loading step.

Table 6
Mechanical properties used in mesoscopic FE analysis and PUC analysis of T700S/2592 laminates.

Mesoscopic FE analysis	
Longitudinal Young's modulus E_1	115 GPa[a]
Transverse Young's modulus E_2, E_3	7.74 GPa[a]
Shear modulus G_{12}, G_{13}	3.54 GPa[a]
Shear modulus G_{23}	2.78 GPa[a]
Poisson's ratio ν_{12}, ν_{13}	0.315[a]
Poisson's ratio ν_{23}	0.394[a]
Coefficient of thermal expansion for longitudinal direction α_1	0.4×10^{-6}/K[b]
Coefficient of thermal expansion for transverse direction α_2, α_3	36×10^{-6}/K [b]
Temperature change ΔT	−100 K
Microscopic PUC analysis	
Fiber longitudinal Young's modulus E_L	230 GPa[c]
Fiber transverse Young's modulus E_T	16.5 GPa[b]
Fiber longitudinal Poisson's ratio ν_L	0.20[b]
Fiber transverse Poisson's ratio ν_T	0.45[b]
Fiber's coefficient of thermal expansion for longitudinal direction α_L	-1.1×10^{-6}/K[b]
Fiber's coefficient of thermal expansion for transverse direction α_T	10×10^{-6}/K[b]
Matrix Young's modulus E_m	3.4 GPa[b]
Matrix Poisson's ratio ν_m	0.31[b]
Matrix's coefficient of thermal expansion α_m	60×10^{-6}/K[b]
Fiber volume fraction V_f	51%[a]
Fiber diameter d_f	7 μm[c]

[a] Properties were determined from tensile tests of unidirectional laminates listed in Table 5.
[b] Properties were taken from Okabe et al. (2015).
[c] Properties were taken from Datasheet (Toray Composite Materials America, 2018a).

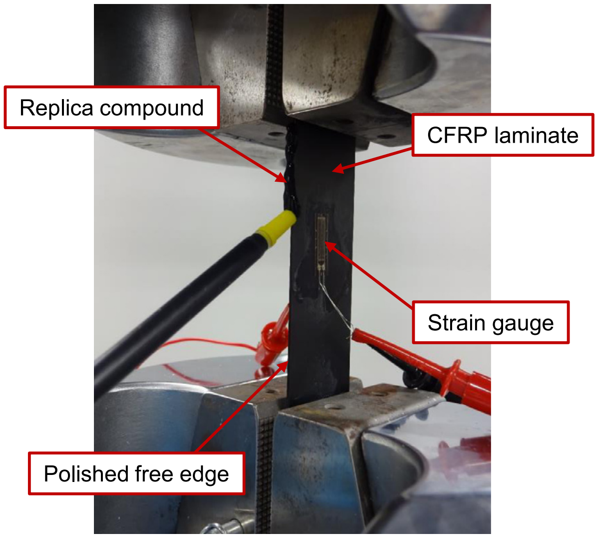

Fig. 11. Interrupted tensile tests of laminated composites with the replication technique.

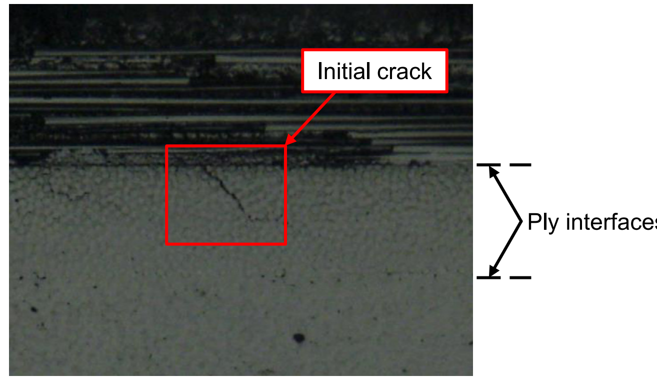

(a) Replica observation of initial crack near interlaminar area on free edge

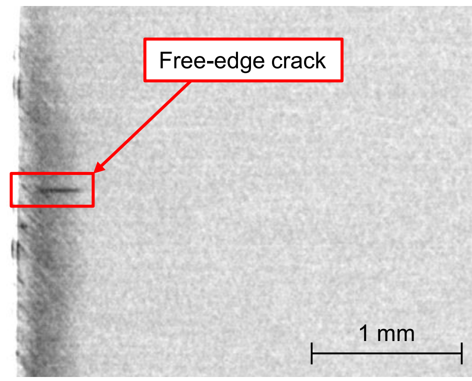

(b) X-ray CT image of free-edge cracks immediately after free-edge crack initiation

Fig. 13. Microscopic crack observations by replication technique and X-ray CT in quasi-isotropic laminate.

Fig. 12 by red dashed dotted lines. In the microscopic replica observation in the experiment, all initial cracks occurred at the interlaminar area on the free edge, as seen in Fig. 13(a), and then a crack encompassing the entire thickness of the ply on the free edge was generated. It should be noted that we observed both the full-thickness crack generated from the initial interface crack and that generated independently from the initial interface crack. In addition, no evident delamination was seen near the initial cracks and the subsequent free-edge cracks. In the X-ray CT experiments, as shown in Fig. 13(b), the generated free-edge crack did not grow to a full-width crack at the free-edge cracking strain. This cracking behavior agrees with previous experimental reports, which stated that thin-ply quasi-isotropic laminates can suppress immediate full-width transverse crack formation after free-edge crack initiation (Kohler et al., 2019). This experimental observation was supported by the analytical prediction using the energy criterion. Because a full-width transverse crack was not observed in the experiments, identifying the critical energy release rate by comparison of prediction of the energy criterion with experimental values was inappropriate. Hence, the typical value of an energy release rate of 200 J/m^2 was employed for the discussion below. The energy criterion using the typical energy release rate of 200 J/m^2 overestimated the free-edge cracking strains of Fig. 12(a) and (b) and predicted no transverse crack formation for the applied strain of 2%, as shown in Fig. 12(c). These results indicate that the ply thickness of 0.10 mm was thin enough to suppress immediate full-width transverse crack formation in this case. Note that when a full-width transverse crack is formed in the present case with large applied strains shown in Fig. 12, delamination can also be formed because of the large stress in the laminate. This case can be predicted by analytical models proposed in literature (Nairn and Hu, 1992; Carraro et al., 2017).

In the case of multiscale analysis, the predicted initial cracking strains on the free edge agreed with the experimental results.

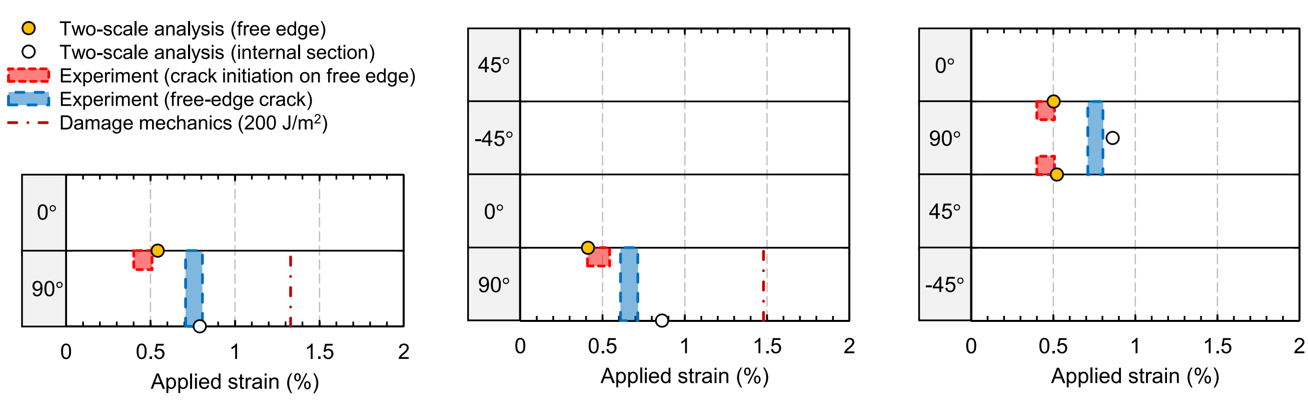

(a) $[0/90]_s$ (b) $[\pm 45/0/90]_s$ (c) $[0/90/\pm 45]_s$

Fig. 12. Comparison of predicted initial cracking strains with experiment results obtained for T700S/2592 laminates.

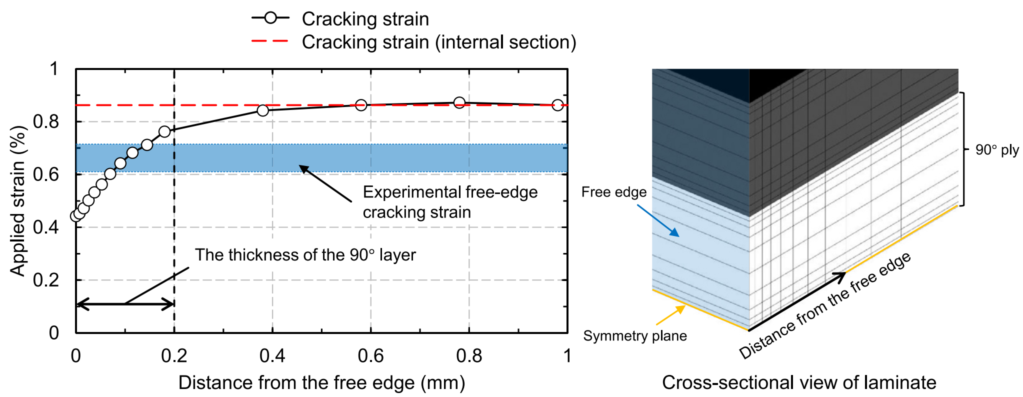

(a) $[\pm 45/0/90]_s$

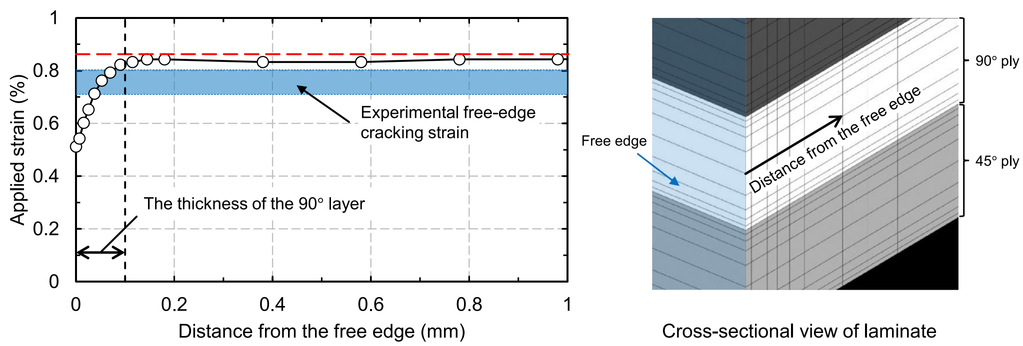

(b) $[0/90/\pm 45]_s$

Fig. 14. Cracking strain distribution along the midplane of the 90° layer of quasi-isotropic laminates.

In addition, although transverse cracks did not propagate over the width of the laminates, the simulated cracking strains at the internal section agreed reasonably with the experimental free-edge cracking strains.

To discuss the free-edge cracking event in further detail, additional FE analysis was conducted on the midplane of the 90° ply. Fig. 14 shows the cracking strain distribution obtained by two-scale analysis on the midplane of the 90° layer of the quasi-isotropic laminates. The horizontal axis represents the depth of analysis points from the free edge, and the vertical axis illustrates crack onset strains at each analysis point. The cracking strain at the internal section is depicted by red dashed lines. As shown in the figure, the cracking strains near the free edge converged on the internal cracking strain, and the convergence distance from the free edge was comparable with the thickness of several plies. Assuming that a free-edge crack is formed as a semicircular crack, the crack initiation at the distance equal to the thickness of the 90° layer can be considered as a simplified criterion of the free-edge crack initiation. In Fig. 14, a depth equal to the 90° layer thickness and the experimental free-edge cracking strains, which are also shown in Fig. 12, are illustrated by black dashed lines and blue bands, respectively. Comparison of the results of the two-scale analysis and the experiments showed that the predicted cracking strains at the depth equal to the thickness of the 90° layer reasonably reproduced the experimental onset strains despite our simplified assumption.

To validate the developed two-scale approach in more detail, the influence of fiber arrangement in PUC analysis on cracking strains was examined. Fig. 15 shows the unit cell models used for the validation of the fiber arrangement effect. The unit cells with randomly distributed fibers were generated by following literature (D'Mello et al., 2016). Note that Model I is identical to the unit cell model shown in Fig. 4, hence, two additional models were analyzed for the validation. Fig. 16 compares predicted cracking strains obtained by the two-scale analysis using three different unit cells. The circular, square, and diamond symbols represent the predicted cracking strains of Model I, II, and III, respectively. Although the predicted cracking strains were slightly affected by the fiber arrangement, the cracking sequence, which is crack initiation at the free-edge interlaminar area followed by cracking at internal section, was identical among the three cases. This result indicates that the prediction capability of the developed two-scale analysis was insensitive to the fiber arrangement of unit cells.

Moreover, we evaluated the influence of the constitutive model of mesoscopic analysis and the constitutive and failure models of PUC analysis on crack prediction of quasi-isotropic laminates. In mesoscopic analysis, each lamina was modeled as an orthotropic elastic body. In PUC analysis, based on the discussion of Okabe et al. (2015), the matrix phase of a unit cell was assumed to be an elastic body and crack initiation was modeled by the following dilatational energy density (DED) criterion proposed by Asp et al. (1996a):

$$U_v = \frac{1-2\nu}{6E}(\sigma_1+\sigma_2+\sigma_3)^2. \quad (21)$$

Here, U_v is the dilatational energy density, E is Young's modulus, ν is Poisson's ratio, and σ_i is the principal stress. A matrix crack was assumed to occur when U_v reached its critical value U_v^{crit}. We employed $U_v^{crit} = 1.1$ MPa, referring to literature (Okabe et al., 2015). Fig. 17 compares the predicted cracking strains obtained by the elastic modeling case with the nonlinear modeling case and experiments presented in Fig. 12. The modeling strategies of cases

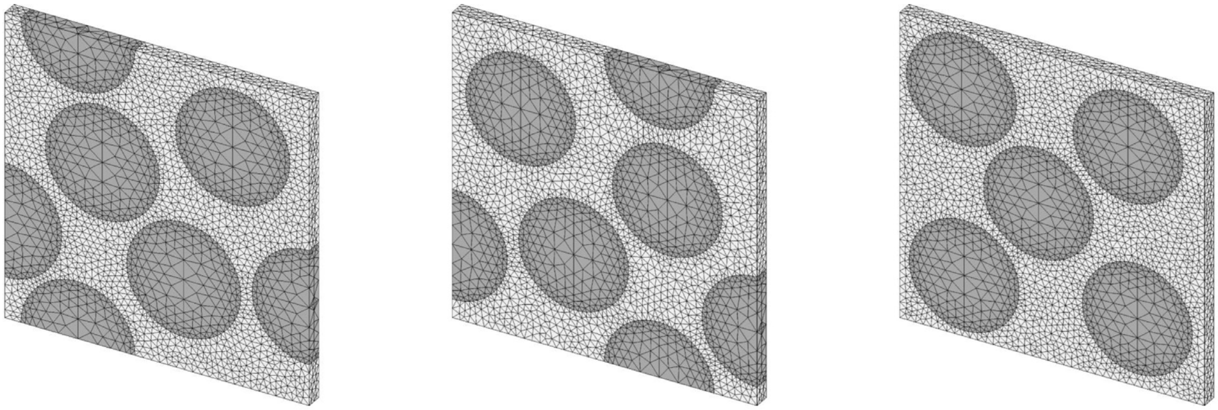

(a) Model I (b) Model II (c) Model III

Fig. 15. Unit cell models for the validation of fiber arrangement effect.

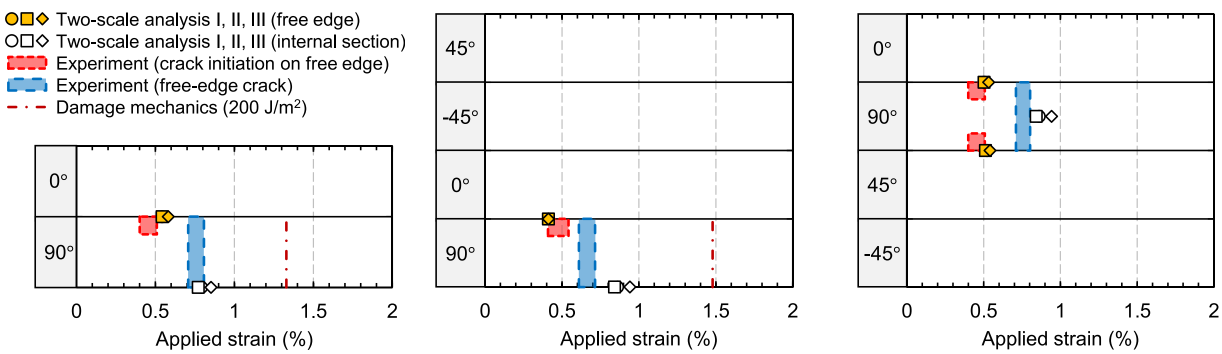

(a) $[0/90]_s$ (b) $[\pm 45/0/90]_s$ (c) $[0/90/\pm 45]_s$

Fig. 16. Comparison of predicted cracking strains obtained by PUC analysis using three fiber configurations.

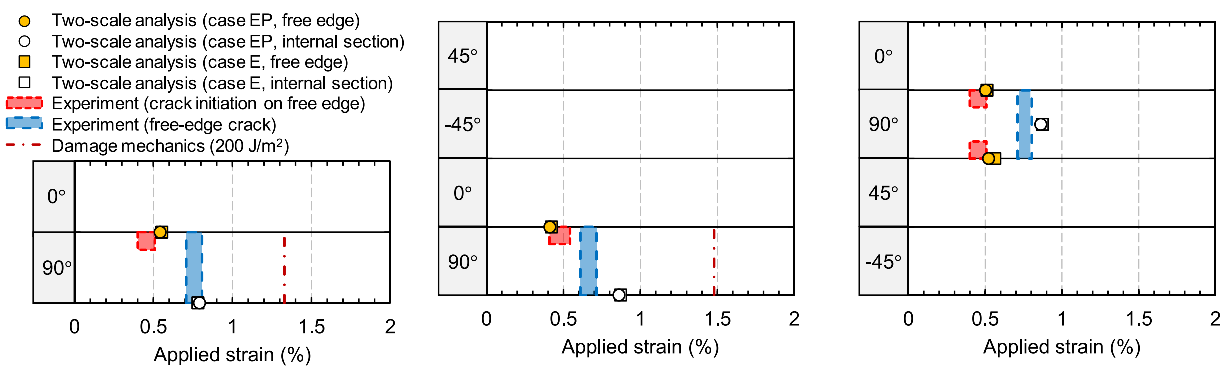

(a) $[0/90]_s$ (b) $[\pm 45/0/90]_s$ (c) $[0/90/\pm 45]_s$

Fig. 17. Effect of constitutive and failure modeling of two-scale analysis on predicted cracking strains. The difference between the cases EP and E is constitutive and failure models in two-scale analysis and summarized in Table 7.

EP and E, and detailed computational results are summarized in Table 7. As shown in the results, the predicted results of case E modeling were practically identical to those of case EP modeling. These results indicate that, if the transverse cracks in the 90° layer of quasi-isotropic laminates are analyzed, the effect of plastic deformation on the mesoscopic and microscopic scales on crack prediction is negligible, and hydrostatic stress-induced cracking has the dominant effect on crack prediction.

Finally, the results of our two-scale analysis were interpreted along with the transverse cracking process described in Fig. 1. Our microscopic PUC analysis only modeled the nucleation of microcracks in stage 1 and successfully reproduced the initial cracking strains near the free-edge interlaminar area. In addition, two-scale analysis of the internal section of laminates reasonably captured the free-edge cracking, which can be caused by coalescence of microcracks in stage 2, despite the simplified modeling in PUC analy-

Table 7
Comparison of predicted cracking strains on different constitutive and failure modeling strategies of two-scale analysis.

Laminate configuration	Location	Case EP Mesoscale: elasto-plastic PUC: elasto-viscoplastic Failure: Christensen	Case E Mesoscale: elastic PUC: elastic Failure: DED
$[0/90]_s$	0/90 interface at free edge (%)	0.542	0.552
	Internal section (%)	0.792	0.782
$[\pm 45/0/90]_s$	0/90 interface at free edge (%)	0.412	0.422
	Internal section (%)	0.862	0.872
$[0/90/\pm 45]_s$	0/90 interface at free edge (%)	0.502	0.513
	90/45 interface at free edge (%)	0.522	0.563
	Internal section (%)	0.862	0.873

sis. As shown in Fig. 14, the cracking strains on the midplane of 90° plies converged near the free edge of the laminates where the constraining effect by neighboring plies is weaker than that offered by the internal section. Crack initiation at the convergence point can be considered as a sufficient condition for a free-edge crack formation assuming the free-edge crack formed as a semicircular shape crack. Hence, the prediction at the internal section acted as a representative point for the free-edge crack prediction. The full-width transverse crack formation in stage 3 could be predicted for the case of T800H/3900-2 only by PUC analysis. In this case, the 90° layer was thick enough to satisfy the energy criterion immediately after stress-based crack nucleation.

One possible approach to predict the entire process of transverse cracking is micro-mechanical FE modeling, in which a unit cell consisting of fibers and matrix is embedded between homogenized plies (Arteiro et al., 2014; Herráez et al., 2015). In this kind of modeling, matrix damage is modeled by continuum damage mechanics and crack band (Bažant and Oh, 1983) models and all cracking stages presented in Fig. 1 can be captured. However, application of this strategy is still limited to two-dimensional cases because of the appreciable computational costs involved. Future development of a high-performance computing infrastructure will help us establish a detailed multiscale FE approach for transverse crack prediction. Our future work will involve detailed discussion of the full transverse cracking process obtained computationally, although the major cracking process for tensile loading cases presented here will not be affected by the investigation.

5. Conclusions

In this work, a multiscale study on matrix crack initiation in the 90° ply of cross-ply and quasi-isotropic laminates was undertaken. The laminate-scale deformation behavior was reproduced by a mesoscopic FE analysis that assumed each lamina to be a homogeneous anisotropic elasto-plastic body. The material nonlinearity and the process of crack formation on the fiber-diameter scale were simply modeled by an elasto-viscoplastic constitutive model and a two-parameter stress-based failure criterion in a microscale-level FEA in a PUC. Our multiscale formulation, combining mesoscopic and microscopic FE analyses, indicated that the cracking sequence in the 90° ply in quasi-isotropic laminates was identical to the one in cross-ply laminates. Cracks in the 90° layer initiated at the interlaminar area on the free edge, followed by microcracks at the internal section. In addition to the computational work, detailed microscopic observation of crack initiation was conducted on cross-ply and quasi-isotropic laminates, using the in situ replication technique and ex situ X-ray computed tomography. Comparison of simulated results with microscopic observations demonstrated that our multiscale analysis can reasonably predict the initial microcrack induced near the free-edge interlaminar area and the free-edge crack. In addition, the sensitivity to fiber arrangement and the influence of constitutive and failure modeling of the two-scale analysis on predicted results was examined. It showed that the prediction of the developed two-scale approach was insensitive to the fiber configuration of unit cells. If the transverse cracks in the 90° layer of quasi-isotropic laminates are predicted, the results indicated that inelastic deformation on the mesoscopic and microscopic scales did not affect the crack prediction and that the hydrostatic stress-induced cracking was influential in crack prediction. The reported method shows the damage progress wherein microcrack nucleation and coalescence followed by the full-width transverse cracking in laminated composites that can be seen under tensile loading conditions.

Declaration of Competing Interest

The authors declare that they have no known competing financial interests or personal relationships that could have appeared to influence the work reported in this paper.

CRediT authorship contribution statement

Yuta Kumagai: Software, Validation, Formal analysis, Investigation, Data curation, Writing - original draft, Writing - review & editing, Visualization. **Sota Onodera:** Validation, Formal analysis, Investigation, Writing - review & editing. **Marco Salviato:** Writing - review & editing. **Tomonaga Okabe:** Conceptualization, Resources, Writing - review & editing, Supervision.

Acknowledgements

This work was supported by Council for Science, Technology and Innovation (CSTI), the Cross-ministerial Strategic Innovation Promotion Program (SIP), "Materials Integration" for Revolutionary Design System of Structural Materials (Funding agency: JST). The authors would like to acknowledge the crucial encouragement and support received from the University of Washington–Tohoku University: Academic Open Space (UW–TU: AOS). This work was also supported by Japan Society for the Promotion of Science (JSPS) Grant-in-Aid for JSPS Research Fellow Numbers JP17J02004 and JP18J20899. The authors thank Toray Industries, Inc. and Dr. Nobuo Takeda, Dr. Shu Minakuchi, and Mr. Shinsaku Hisada of the University of Tokyo for their support in specimen fabrication. The authors would like to thank Editage (www.editage.com) for English language editing.

Appendix A

In this section, the compatibility between mesoscopic analysis and microscopic PUC analysis was examined, and the influence of their mechanical properties on the prediction of crack initiation was evaluated. First, the two-scale analysis was applied to tensile tests of unidirectional laminates under off-axis loading to present compatibility between mesoscopic and microscopic analysis, using

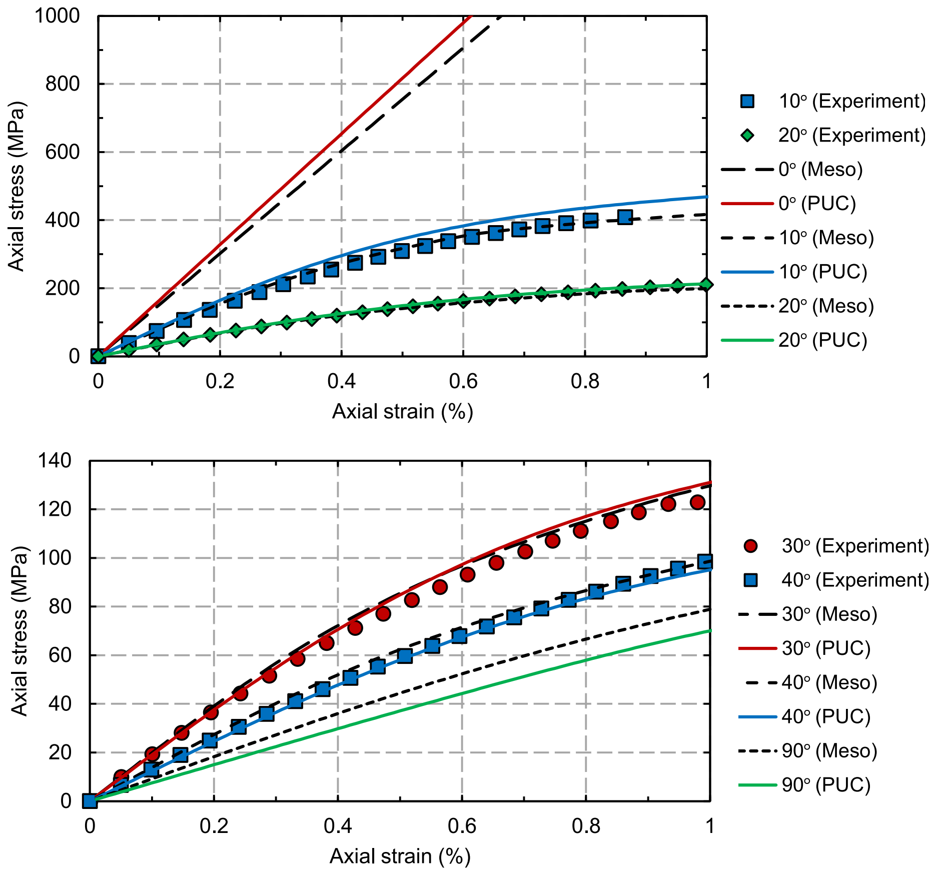

Fig. A1. Comparison of stress–strain curves obtained by mesoscopic laminate analysis, PUC analysis, and experiment of unidirectional laminates (experimental data taken from Yoshioka et al. (2016)).

Table A1
Mechanical properties used in mesoscopic FE analysis and PUC analysis of T800H/3900-2B laminates. Mechanical properties of fiber and matrix were modified from Table 4 to improve compatibility between mesoscopic and PUC analyses.

Mesoscopic FE analysis[a]	
Longitudinal Young's modulus E_1	151 GPa
Transverse Young's modulus E_2, E_3	9.16 GPa
Shear modulus G_{12}, G_{13}	4.62 GPa
Shear modulus G_{23}	2.55 GPa
Poisson's ratio ν_{12}, ν_{13}	0.302
Poisson's ratio ν_{23}	0.589
Coefficient of thermal expansion for longitudinal direction α_1	0×10^{-6}/K
Coefficient of thermal expansion for transverse direction α_2, α_3	33×10^{-6}/K
Temperature change ΔT	−150 K
Microscopic PUC analysis	
Fiber longitudinal Young's modulus E_L	260 GPa[b]
Fiber transverse Young's modulusE_T	19.5 GPa[c]
Fiber longitudinal Poisson's ratio ν_L	0.17[c]
Fiber transverse Poisson's ratio ν_T	0.46[c]
Fiber's coefficient of thermal expansion for longitudinal direction α_L	-1.1×10^{-6}/K[c]
Fiber's coefficient of thermal expansion for transverse direction α_T	10×10^{-6}/K[c]
Matrix Young's modulus E_m	3.8 GPa[d]
Matrix Poisson's ratio ν_m	0.38[c]
Matrix's coefficient of thermal expansion α_m	60×10^{-6}/K[c]
Fiber volume fraction V_f	56%
Fiber diameter d_f	5 µm[e]

[a] All mechanical properties for mesoscopic analysis were taken from Shigemori et al. (2014).
[b] Properties were taken from Tane et al. (2019).
[c] Properties were taken from Yoshioka et al. (2016).
[d] Assumed value.
[e] Properties were taken from Datasheet (Toray Composite Materials America, 2018b).

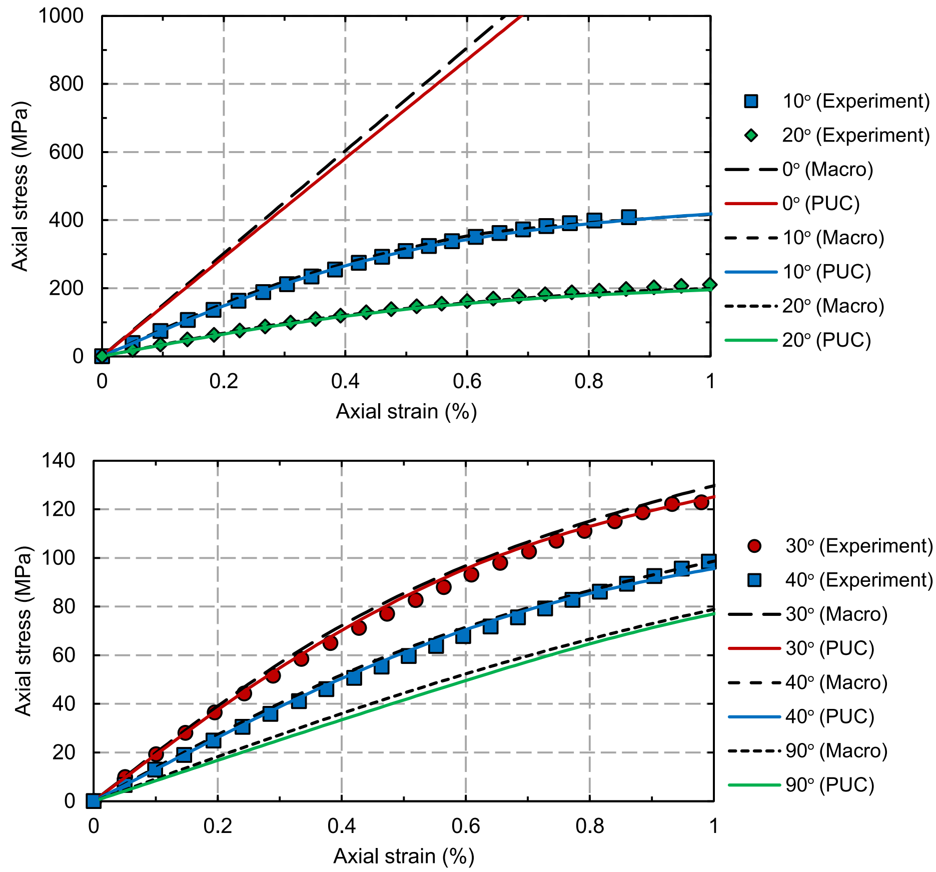

Fig. A2. Comparison of stress–strain curves obtained by mesoscopic laminate analysis, PUC analysis, and experiment of unidirectional laminates after material constant fitting (experimental data taken from Yoshioka et al. (2016)).

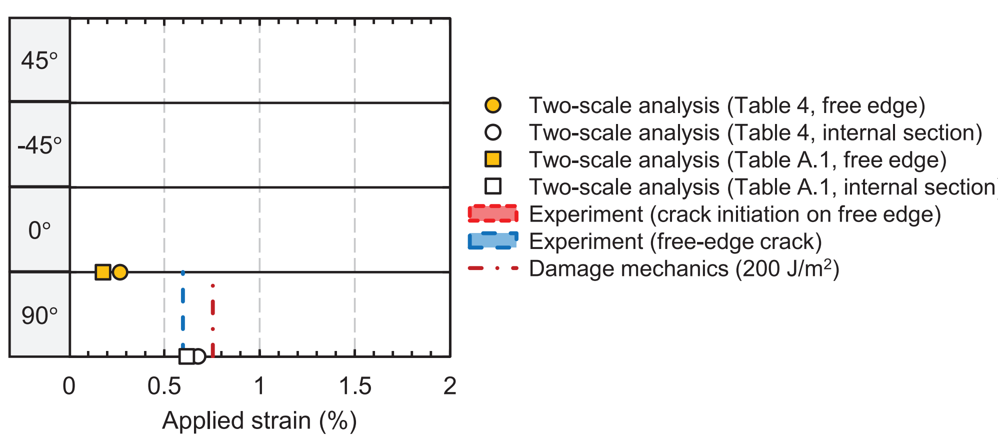

Fig. A3. Influence of mechanical properties used for PUC analysis on the predicted cracking strains. Two-scale analysis was carried out for [± 45/0/90]$_s$ laminate with T800H/3900-2 case as shown in Fig. 7(e). The blue dashed lines show experimentally characterized strains of transverse cracking (Kobayashi et al., 2000; Ogihara et al., 2001). Simulated results using properties from Tables 4 and A.1 are represented by circular and square symbols, respectively. (For interpretation of the references to color in this figure legend, the reader is referred to the web version of this article.)

the parameters listed in Table 4. Fig. A.1 shows the comparison of stress–strain curves obtained by mesoscopic analysis and microscopic PUC analysis. In the figure, the dashed lines represent the results of mesoscopic analysis and the solid lines illustrate the results of PUC analysis. Moreover, experimental data available in literature (Yoshioka et al., 2016) is depicted by symbols for the purpose of validation. The compatibility between mesoscopic and PUC analyses can be improved by fitting the mechanical properties.

Subsequently, the fiber longitudinal Young's modulus E_L and the matrix Young's modulus E_m were adjusted to improve the compatibility of the two FE analyses. The value $E_L = 260$ GPa was determined based on experimental measurement of elastic constants of carbon fibers reported in literature (Tane et al., 2019) and the value $E_m = 3.8$ GPa was identified through the comparison of stress–strain curves between mesoscopic and PUC analyses. The mechanical properties obtained after stress–strain curve fitting are summarized in Table A.1. Fig. A.2 compares the stress–strain curves of the off-axis tensile tests of unidirectional laminate obtained by mesoscopic and PUC analyses. By employing mechanical properties listed in Table A.1, the compatibility between mesoscopic and PUC analyses was improved.

Finally, the influence of the compatibility between mesoscopic and PUC analyses on the prediction of the crack initiation was evaluated by predicting cracking strains on the 90° layer of quasi-isotropic laminate. Fig. A.3 compares the predicted cracking strains of $[\pm 45/0/90]_s$ laminate in the case of T800H/3900-2 obtained using the mechanical properties listed in Tables 4 and A.1. Although the predicted cracking strains were marginally affected by the mechanical properties, the cracking sequence, which is the crack initiation at the free-edge interlaminar area followed by cracking at the internal section, was identical between the two cases. This result indicates that the compatibility between mesoscopic analysis and microscopic PUC analysis was sufficient for the developed two-scale analysis in the present case.

Appendix B

An analytical model (Onodera and Okabe, 2019) used to predict steady-state cracking strain in the 90° ply of quasi-isotropic laminates is briefly described here. Steady-state ply cracking is a fracture mode wherein a ply crack propagates over the width of the specimen under constant thermo-mechanical loading. The model used here assumes that a new ply crack is generated between two pre-existing cracks with a crack spacing $4l$: thus, a unit cell of a target ply shown in Fig. B.1 was used for the prediction. The energy release rate associated with new crack formation is expressed as:

$$\Gamma_k(\rho) = -\frac{U_k(\rho/2) - 2U_k(\rho)}{t_k}, \tag{B.1}$$

where $U_k(\rho)$ is the strain energy of the kth ply of N-ply laminate calculated on the unit cell with crack spacing $2l$ and ply thickness t_k and ρ is the ply crack density and can be defined as $\rho = 1/(2l)$. The strain energy $U_k(\rho)$ is given by the following equation:

$$U_k(\rho) = \frac{t_L}{2\rho}\{\bar{\boldsymbol{\sigma}}_L - \bar{\boldsymbol{\sigma}}_{th}\}^T \bar{\boldsymbol{S}}_L \{\bar{\boldsymbol{\sigma}}_L - \bar{\boldsymbol{\sigma}}_{th}\}. \tag{B.2}$$

Here, $\bar{\boldsymbol{\sigma}}_L$ is the applied stress of the laminate, $\bar{\boldsymbol{\sigma}}_{th}$ is the laminate stress that removes the contribution of the thermal residual stress of the kth ply from $U_k(\rho)$, t_L is the laminate thickness, and $\bar{\boldsymbol{S}}_L$ is the effective compliance matrix of the laminate with ply cracks. $\bar{\boldsymbol{S}}_L$ can be calculated using the three-dimensional laminate theory (Gudmundson and Zang, 1993) and the continuum damage mechanics based on the effective stiffness matrix $\boldsymbol{C}$ as described in literature (Onodera and Okabe, 2019). Detailed formulation of the analytical crack prediction model can be found in literature (Onodera and Okabe, 2019).

Steady-state ply cracking analysis of the laminate with arbitrary lay-ups was conducted by the following procedure. First, the energy release rate of each ply, Γ_k, according to Eq. (B.1) was calculated for the applied laminate stress $\bar{\boldsymbol{\sigma}}_L$ as a function of the ply crack density ρ, assuming that cracks are formed only in the kth ply. Then, the critical applied laminate stress associated with kth ply cracking, $\bar{\boldsymbol{\sigma}}_L^{c,k}$, was determined as the applied laminate stress where $\max_{\rho}[\Gamma_k(\rho)]$ is equal to the critical energy release rate Γ_c. Finally, the initial steady-state cracking strain of laminate was determined as the strain at which a ply crack was formed in a ply subjected to the minimum ply cracking applied stress $\min_k[\bar{\boldsymbol{\sigma}}_L^{c,k}]$.

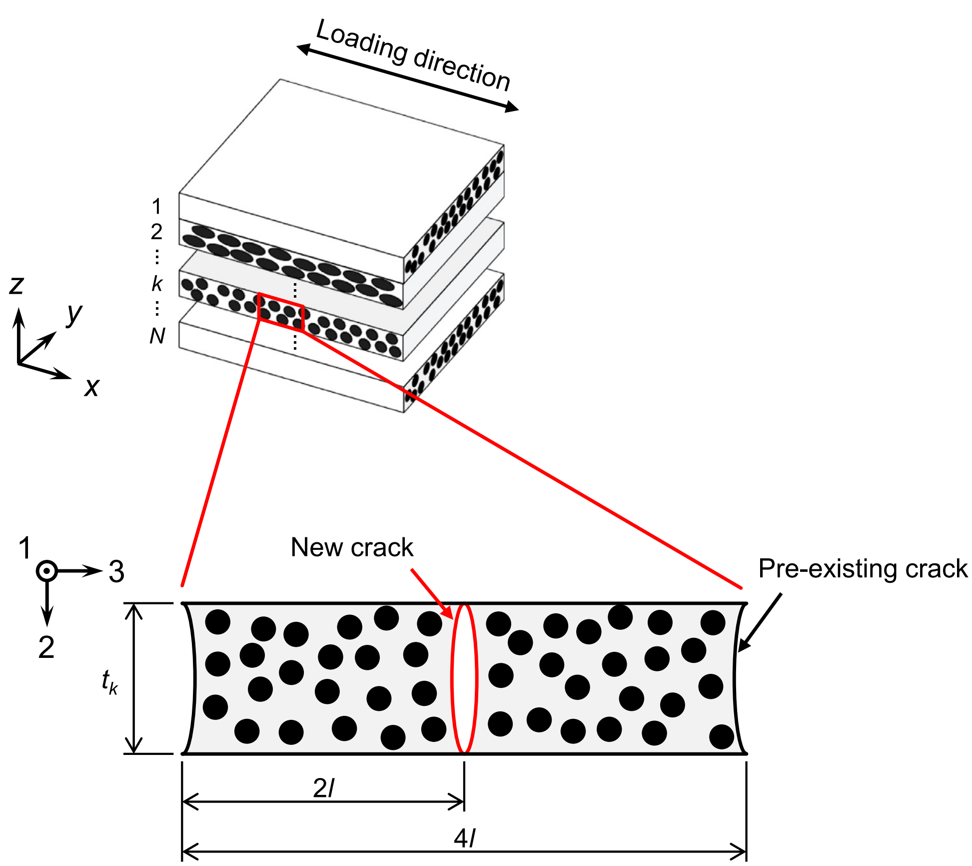

Fig. B1. Representative unit cell used for analytical prediction of steady-state cracking in kth ply of laminate.

References

Aratama, S., Hashizume, R., Takenaka, K., Koga, K., Tsumura, Y., Miyake, T., Nishikawa, M., Hojo, M., 2016. Microscopic observation of voids and transverse crack initiation in CFRP laminates. Adv. Compos. Mater. 25, 115–130. doi:10.1080/09243046.2016.1206720.

Arteiro, A., Catalanotti, G., Melro, A.R., Linde, P., Camanho, P., 2014. Micromechanical analysis of the in situ effect in polymer composite laminates. Compos. Struct. 116, 827–840. doi:10.1016/j.compstruct.2014.06.014.

Asp, L.E., Berglund, L., Talreja, R., 1996. A criterion for crack initiation in glassy polymers subjected to a composite-like stress state. Compos. Sci. Technol. 56, 1291–1301. doi:10.1016/S0266-3538(96)00090-5.

Asp, L.E., Berglund, L., Talreja, R., 1996. Prediction of matrix-initiated transverse failure in polymer composites. Compos. Sci. Technol. 56, 1089–1097. doi:10.1016/0266-3538(96)00074-7.

Bai, X., Bessa, M.A., Melro, A.R., Camanho, P.P., Guo, L., Liu, W.K., 2015. High-fidelity micro-scale modeling of the thermo-visco-plastic behavior of carbon fiber polymer matrix composites. Compos. Struct. 134, 132–141. doi:10.1016/j.compstruct.2015.08.047.

Bažant, Z.P., Oh, B.H., 1983. Crack band theory for fracture of concrete. Matér. Constr. 16, 155–177. doi:10.1007/BF02486267.

Bažant, Z.P., Pijaudier-Cabot, G., 1988. Nonlocal continuum damage, localization instability and convergence. J. Appl. Mech. 55, 287–293. doi:10.1115/1.3173674.

Bornert, M., Brémand, F., Doumalin, P., Dupré, J.C., Fazzini, M., Grédiac, M., Hild, F., Mistou, S., Molimard, J., Orteu, J.J., Robert, L., Surrel, Y., Vacher, P., Wattrisse, B., 2009. Assessment of digital image correlation measurement errors: methodology and results. Exp. Mech. 49, 353–370. doi:10.1007/s11340-008-9204-7.

Carraro, P., Quaresimin, M., 2015. A stiffness degradation model for cracked multidirectional laminates with cracks in multiple layers. Int. J. Solids Struct. 58, 34–51. doi:10.1016/j.ijsolstr.2014.12.016.

Carraro, P.A., Novello, E., Quaresimin, M., Zappalorto, M., 2017. Delamination onset in symmetric cross-ply laminates under static loads: theory, numerics and experiments. Compos. Struct. 176, 420–432. doi:10.1016/j.compstruct.2017.05.030.

Christensen, R.M., 2013. The Theory of Materials Failure. Oxford University Press doi:10.1093/acprof:oso/9780199662111.001.0001.

Daniel, I.M., Ishai, O., 1994. Engineering Mechanics of Composite Materials. Oxford University Press, New York.

D'Mello, R., Maiarù, M., Waas, A.M., 2016. Virtual manufacturing of composite aerostructures. Aeron. J. 120, 61–81. doi:10.1017/aer.2015.19.

Elnekhaily, S.A., Talreja, R., 2018. Damage initiation in unidirectional fiber composites with different degrees of nonuniform fiber distribution. Compos. Sci. Technol. 155, 22–32. doi:10.1016/j.compscitech.2017.11.017.

Elnekhaily, S.A., Talreja, R., 2019. Effect of axial shear and transverse tension on early failure events in unidirectional polymer matrix composites. Compos. Part A 119, 275–282. doi:10.1016/j.compositesa.2019.01.031.

Fiedler, B., Hojo, M., Ochiai, S., Schulte, K., Ando, M., 2001. Failure behavior of an epoxy matrix under different kinds of static loading. Compos. Sci. Technol. 61, 1615–1624. doi:10.1016/S0266-3538(01)00057-4.

Gudmundson, P., Zang, W., 1993. An analytic model for thermoelastic properties of composite laminates containing transverse matrix cracks. Int. J. Solids Struct. 30, 3211–3231. doi:10.1016/0020-7683(93)90110-S.

Hart-Smith, L.J., 2014. Is there really no need to be able to predict matrix failures in fibre-polymer composite structures? Part 1: explanation of fatal flaws in existing theories. Aust. J. Mech. Eng. 12, 139–159. doi:10.7158/M12-AGM01.2014.12.2.

Herráez, M., Mora, D., Naya, F., Lopes, C.S., González, C., LLorca, J., 2015. Transverse cracking of cross-ply laminates: acomputational micromechanics perspective. Compos. Sci. Technol. 110, 196–204. doi:10.1016/j.compscitech.2015.02.008.

Higuchi, R., Okabe, T., Nagashima, T., 2017. Numerical simulation of progressive damage and failure in composite laminates using XFEM/CZM coupled approach. Compos. Part A 95, 197–207. doi:10.1016/j.compositesa.2016.12.026.

Hobbiebrunken, T., Hojo, M., Adachi, T., De Jong, C., Fiedler, B., 2006. Evaluation of interfacial strength in CF/epoxies using FEM and in-situ experiments. Compos. Part A 37, 2248–2256. doi:10.1016/j.compositesa.2005.12.021.

ASTM International, 2012. Intel math kernel library documentation. https://software.intel.com/en-us/articles/intel-math-kernel-library-documentation/. (Accessed 27 October 2019).

International, A., 2012. Standard practice for production and evaluation of field metallographic replicas. Doi: 10.1520/E1351-01R12.

Kobayashi, S., Ogihara, S., Takeda, N., 2000. Experimental characterization of the effects of stacking sequence on the transverse crack behavior in quasi-isotropic interleaved CFRP laminates. Adv. Compos. Mater. 9, 241–251. doi:10.1163/15685510051033449.

Kohler, S., Cugnoni, J., Amacher, R., Botsis, J., 2019. Transverse cracking in the bulk and at the free edge of thin-ply composites: experiments and multiscale modelling. Compos. Part A 124, 105468. doi:10.1016/j.compositesa.2019.05.036.

Kumagai, Y., Higuchi, R., Aoyagi, Y., Okabe, T., Yoshioka, K., 2017. Effect of macroscopic nonlinear behavior and microscopic failure criteria on prediction of initial matrix cracking in CFRP laminates. Materials System 35, 19–27. (in Japanese)

Lecomte-Grosbras, P., Paluch, B., Brieu, M., 2013. Characterization of free edge effects: influence of mechanical properties, microstructure and structure effects. J. Compos. Mater. 47, 2823–2834. doi:10.1177/0021998312458817.

Lecomte-Grosbras, P., Paluch, B., Brieu, M., Saxcé, G.D., Sabatier, L., 2009. Interlaminar shear strain measurement on angle-ply laminate free edge using digital image correlation. Compos. Part A 40, 1911–1920. doi:10.1016/j.compositesa.2009.07.011.

Lu, X., Chen, B.Y., Tan, V.B.C., Tay, T.E., 2018. A separable cohesive element for modelling coupled failure in laminated composite materials. Compos. Part A 107, 387–398. doi:10.1016/j.compositesa.2018.01.014.

Lukaszewicz, D.H.J., 2013. Automotive composite structures for crashworthiness. In: Elmarakbi, A. (Ed.), Advanced Composite Materials for Automotive Applications. John Wiley & Sons Ltd, pp. 99–127. doi:10.1002/9781118535288.ch5

Maragoni, L., Talreja, R., 2019. Transverse crack formation in unidirectional plies predicted by means of a percolation concept. Compos. Part A 117, 317–323. doi:10.1016/j.compositesa.2018.11.025.

Matsuda, T., Ohno, N., Tanaka, H., Shimizu, T., 2002. Homogenized in-plane elastic-viscoplastic behavior of long fiber-reinforced laminates. JSME Int. J. Ser. A Solid Mech. Mater. Eng. 45, 538–544. doi:10.1299/jsmea.45.538.

Melro, A.R., Camanho, P.P., Andrade Pires, F.M., Pinho, S.T., 2013. Micromechanical analysis of polymer composites reinforced by unidirectional fibres: part II-micromechanical analyses. Int. J. Solids Struct. 50, 1906–1915. doi:10.1016/j.ijsolstr.2013.02.007.

Nairn, J.A., Hu, S., 1992. The initiation and growth of delaminations induced by matrix microcracks in laminated composites. Int. J. Fract. 57, 1–24. doi:10.1007/BF00013005.

Naya, F., Herráez, M., Lopes, C., González, C., Van der Veen, S., Pons, F., 2017. Computational micromechanics of fiber kinking in unidirectional FRP under different environmental conditions. Compos. Sci. Technol. 144, 26–35. doi:10.1016/j.compscitech.2017.03.014.

Ogihara, S., Kobayashi, A., Takeda, N., Kobayashi, S., 2000. Damage mechanics analysis of transverse cracking behavior in composite laminates. Int. J. Damage Mech. 9, 113–129. doi:10.1177/105678950000900201.

Ogihara, S., Kobayashi, S., Takeda, N., Kobayashi, A., 2001. Damage mechanics characterization of transverse cracking behavior in high-temperature CFRP laminates. Compos. Sci. Technol. 61, 1049–1055. doi:10.1016/S0266-3538(00)00236-0.

Okabe, T., Imamura, H., Sato, Y., Higuchi, R., Koyanagi, J., Talreja, R., 2015. Experimental and numerical studies of initial cracking in CFRP cross-ply laminates. Compos. Part A 68, 81–89. doi:10.1016/j.compositesa.2014.09.020.

Okabe, T., Nishikawa, M., Takeda, N., 2008. Numerical modeling of progressive damage in fiber reinforced plastic cross-ply laminates. Compos. Sci. Technol. 68, 2282–2289. doi:10.1016/j.compscitech.2008.04.021.

Okabe, T., Nishikawa, M., Toyoshima, H., 2011. A periodic unit-cell simulation of fiber arrangement dependence on the transverse tensile failure in unidirectional carbon fiber reinforced composites. Int. J. Solids Struct. 48, 2948–2959. doi:10.1016/j.ijsolstr.2011.06.012.

Onodera, S., Okabe, T., 2019. Three-dimensional analytical model for effective elastic constants of transversely isotropic plates with multiple cracks: application to stiffness reduction and steady-state cracking of composite laminates. Eng. Fract. Mech. 219, 106595. doi:10.1016/j.engfracmech.2019.106595.

Pagano, N.J., Schoeppner, G.A., Kim, R., Abrams, F.L., 1998. Steady-state cracking and edge effects in thermo-mechanical transverse cracking of cross-ply laminates. Compos. Sci. Technol. 58, 1811–1825. doi:10.1016/S0266-3538(98)00047-5.

Qiao, Y., Deleo, A.A., Salviato, M., 2019. A study on the multi-axial fatigue failure behavior of notched composite laminates. Compos. Part A 127, 105640. doi:10.1016/j.compositesa.2019.105640.

Qiao, Y., Salviato, M., 2019. Micro-computed tomography analysis of damage in notched composite laminates under multi-axial fatigue. arXiv:1910.01670.

Ramberg, W., Osgood, W.R., 1943. Description of Stress–Strain Curves by Three Parameters. National Advisory Committee for Aeronautics Technical Note.

Rana, S., Fangueiro, R. (Eds.), 2016. Advanced Composite Materials for Aerospace Engineering: Processing, properties 605 and applications. Woodhead Publishing. 10.1016/C2014-0-00846-5.

Sato, Y., Okabe, T., Higuchi, R., Yoshioka, K., 2014. Multiscale approach to predict crack initiation in unidirectional off-axis laminates. Adv. Compos. Mater. 23, 461–475. doi:10.1080/09243046.2014.915100.

Scott, A., Sinclair, I., Spearing, S., Thionnet, A., Bunsell, A., 2012. Damage accumulation in a carbon/epoxy composite: comparison between a multiscale model and computed tomography experimental results. Compos. Part A 43, 1514–1522. doi:10.1016/j.compositesa.2012.03.011.

Shigemori, K., Hosoi, A., Fujita, Y., Kawada, H., 2014. Fatigue strength properties of interlaminar toughened CFRP laminates under cyclic loading in the out-of-plane direction. Transactions of the JSME(in Japanese) 80, SMM0087. doi:10.1299/transjsme.2014smm0087. (in Japanese)

Singh, C.V., Talreja, R., 2010. Evolution of ply cracks in multidirectional composite laminates. Int. J. Solids Struct. 47, 1338–1349. doi:10.1016/j.ijsolstr.2010.01.016.

Song, D., Gupta, R., 2012. The use of thermosets in the building and construction industry. In: Guo, Q. (Ed.), Thermosets: Structure, Properties, and Applications. Woodhead Publishing, pp. 165–188. doi:10.1533/9780857097637.2.165

Souza, F.V., Allen, D.H., Kim, Y.R., 2008. Multiscale model for predicting damage evolution in composites due to impact loading. Compos. Sci. Technol. 68, 2624–2634. doi:10.1016/j.compscitech.2008.04.043.

Stenzenberger, H., 1993. Recent developments of thermosetting polymers for advanced composites. Compos. Struct. 24, 219–231. doi:10.1016/0263-8223(93)90216-D.

Su, Z., Tay, T.E., Ridha, M., Chen, B.Y., 2015. Progressive damage modeling of open-hole composite laminates under compression. Compos. Struct. 122, 507–517. doi:10.1016/j.compstruct.2014.12.022.

Sudhir, A., Talreja, R., 2019. Simulation of manufacturing induced fiber clustering and matrix voids and their effect on transverse crack formation in unidirectional composites. Compos. Part A 127, 105620. doi:10.1016/j.compositesa.2019.105620.

Sun, C.T., Chen, J.L., 1989. A simple flow rule for characterizing nonlinear behavior of fiber composites. J. Compos. Mater. 23, 1009–1020. doi:10.1177/002199838902301004.
Talreja, R., Singh, C.V., 2012. Damage and Failure of Composite Materials. Cambridge University Press doi:10.1017/CBO9781139016063.
Tane, M., Okuda, H., Tanaka, F., 2019. Nanocomposite microstructures dominating anisotropic elastic modulus in carbon fibers. Acta Mater. 166, 75–84. doi:10.1016/j.actamat.2018.12.029.
Terada, K., Hirayama, N., Yamamoto, K., Kato, J., Kyoya, T., Matsubara, S., Arakawa, Y., Ueno, Y., Miyanaga, N., 2014. Applicability of micro-macro decoupling scheme to two-scale analysis of fiber-reinforced plastics. Adv. Compos. Mater. 23, 421–450. doi:10.1080/09243046.2014.915098.
Toray Composite Materials America, Inc., 2018a. T700s standard modulus carbon fiber datasheet. https://www.toraycma.com/file_viewer.php?id=5116. (accessed 19 January 2020).
Toray Composite Materials America, Inc., 2018b. T800h intermediate modulus carbon fiber datasheet. https://www.toraycma.com/file_viewer.php?id=5121. (accessed 19 January 2020).
Wang, Y., Burnett, T.L., Chai, Y., Soutis, C., Hogg, P.J., Withers, P.J., 2017. X-Ray computed tomography study of kink bands in unidirectional composites. Compos. Struct. 160, 917–924. doi:10.1016/j.compstruct.2016.10.124.
Weeks, C., Sun, C.T., 1998. Modeling non-linear rate-dependent behavior in fiber-reinforced composites. Compos. Sci. Technol. 58, 603–611. doi:10.1016/S0266-3538(97)00183-8.
Wright, P., Fu, X., Sinclair, I., Spearing, S.M., 2008. Ultra high resolution computed tomography of damage in notched carbon fiber–epoxy composites. J. Compos. Mater. 42, 1993–2002. doi:10.1177/0021998308092211.
Yang, Q., Schesser, D., Niess, M., Wright, P., Mavrogordato, M., Sinclair, I., Spearing, S., Cox, B., 2015. On crack initiation in notched, cross-plied polymer matrix composites. J. Mech. Phys. Solids 78, 314–332. doi:10.1016/j.jmps.2015.01.010.
Yokozeki, T., Ogihara, S., Yoshida, S., Ogasawara, T., 2007. Simple constitutive model for nonlinear response of fiber-reinforced composites with loading-directional dependence. Compos. Sci. Technol. 67, 111–118. doi:10.1016/j.compscitech.2006.03.024.
Yoshioka, K., Kumagai, Y., Higuchi, R., Lee, D., Okabe, T., 2016. Multiscale modeling of failure strain in off-axis tensile testing of UD-CFRP. Materials System 34, 7–13. (in Japanese).
Zhuang, L., Talreja, R., Varna, J., 2018. Transverse crack formation in unidirectional composites by linking of fibre/matrix debond cracks. Compos. Part A 107, 294–303. doi:10.1016/j.compositesa.2018.01.013.